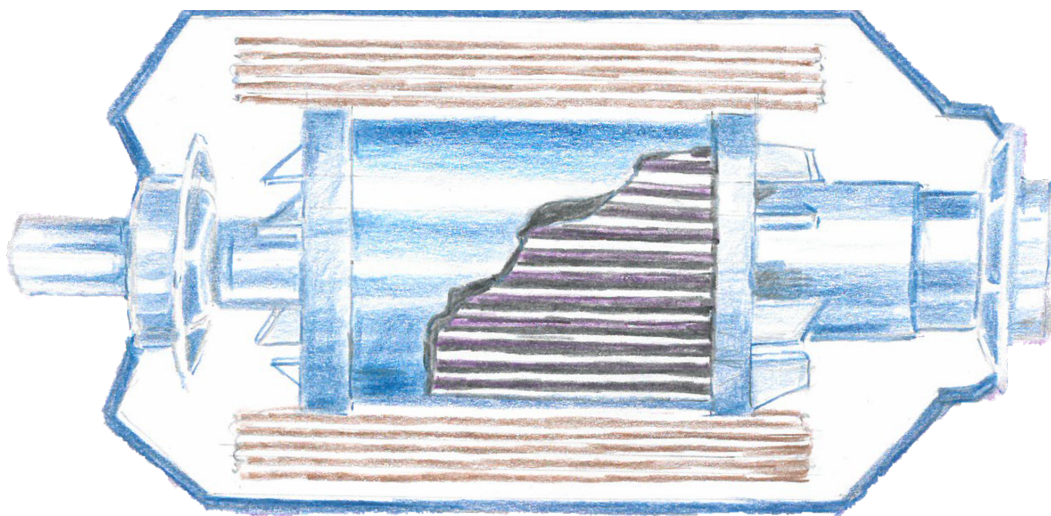




CHALMERS
UNIVERSITY OF TECHNOLOGY



An Induction Machine vs a Standard NdFeB Magnet Machine

A Comparison for Mild Hybrid Vehicle Applications

Master's Thesis in Electric Power Engineering

SEBASTIAN BERGMAN, ANDERS KARLSSON

MASTER'S THESIS 2019

An Induction Machine vs a Standard NdFeB Magnet Machine

A Comparison for Mild Hybrid Vehicle Applications

Sebastian Bergman, Anders Karlsson



CHALMERS
UNIVERSITY OF TECHNOLOGY

Department of Electrical Engineering
Division of Electric Power Engineering
CHALMERS UNIVERSITY OF TECHNOLOGY
Gothenburg, Sweden 2019

An Induction Machine vs a Standard NdFeB Magnet Machine
A Comparison for Mild Hybrid Vehicle Applications
Sebastian Bergman, Anders Karlsson

© Sebastian Bergman, Anders Karlsson, 2019.

Supervisors: Torbjörn Thiringer, Department of Electrical Engineering
Arpit Gupta, Volvo Car Corporation

Examiner: Torbjörn Thiringer, Department of Electrical Engineering

Master's Thesis 2019
Department of Electrical Engineering
Division of Electric Power Engineering
Chalmers University of Technology
SE-412 96 Gothenburg
Telephone +46 31 772 1000

Typeset in L^AT_EX
Gothenburg, Sweden 2019

An Induction Machine vs a Standard NdFeB Magnet Machine
A Comparison for Mild Hybrid Vehicle Applications
SEBASTIAN BERGMAN, ANDERS KARLSSON
Department of Electrical Engineering
Chalmers University of Technology

Abstract

This thesis compares the performance of a 48 V Induction Machine (IM) and a 48 V Permanent Magnet Synchronous Machine (PMSM) in mild hybrid applications, with maximum power around 11 kW. The focus is put on the IM since there is a lack of documentation of its suitability for vehicle application in literature. A minimum loss control algorithm is developed for the IM based on an inverse gamma circuit model with core losses and a 48 V IM hardware design is done in the Finite Element Method (FEM) software Ansys Maxwell. Furthermore, a sustainability comparison is done between the IM and the PMSM, taking economical, environmental and social aspects into consideration.

The result shows in form of efficiency maps and a power map with maximum torque lines that the PMSM has a better overall performance. The maximum torque of the PMSM is 64 Nm in both generation and motoring mode. The IM on the other hand has a maximum torque of 53 Nm in motoring mode and 61 Nm in generation mode. The output power of the IM drops drastically in the field weakening region, only half the maximum output power remains at 6000 rpm. In contrast, the power of the PMSM drops only a few percent at 6000 rpm. Overall drive cycle efficiencies are 88.8-90 % for the PMSM and 83.1-85.6 % for the IM.

The sustainability comparison between the 48 V machines shows small differences in environmental and social aspects, but a great advantage to the IM in terms of material cost. The active material cost for the IM is \$40.3, while the cost for the PMSM is \$82.4. The price difference is mainly due to the NdFeB-magnets used in the PMSM. The Global Warming Potential (GWP) is 42.0 *kg CO₂, eq* for the IM and 48.9 *kg CO₂, eq* for the PMSM. The acidification is 1.53 *kg SO₂, eq* for the IM and 1.64 *kg SO₂, eq* for the PMSM.

Keywords: Mild Hybrid, Electric Vehicle, Electric Machine, PMSM, IM, FEM, Efficiency Maps, Minimum Loss Control.

Acknowledgements

First of all, we would like to express our gratitude towards our main supervisor Torbjörn Thiringer for sharing his knowledge within electrical machines. He has given us valuable insights in many difficult situations and helped the thesis work to always keep moving forward. Furthermore, we would like to thank our supervisor Arpit Gupta at Volvo Car Corporation, as well as everyone within the energy and power ART at Volvo, for their welcoming and helpful attitude and for answering our many questions.

Contents

1	Introduction	1
1.1	Background	1
1.2	Aim	2
1.3	Problem Definition	2
1.4	Scope	3
2	Three Phase Induction Machine Theory	5
2.1	T-model and Analytic Parameter Estimation of the IM	6
2.2	Inverse Gamma Model with Core Losses	9
2.3	Circuit Model Losses	11
2.4	Stray Losses in Rotor Bars	11
3	Case Set-up	13
3.1	Simulation Set-up in Ansys Maxwell	13
3.2	Electric Machine Models	14
3.2.1	The 400 V IM Model	15
3.2.2	The 48 V IM Model - Design Procedure	17
3.2.3	The 48 V PMSM Model	24
3.3	Parameter Identification from the Maxwell Models	25
3.3.1	Identification of L_σ	25
3.3.2	Identification of R_r	25
3.3.3	Identification of L_m and R_c	26
3.3.4	Identification of $P_{r,stray}$	27
3.4	Efficiency Map and Control Algorithm Set-up	28
3.5	Drive Cycle Efficiency Set-up	29
3.6	Sustainability Set-up	32
4	Verification of the Maxwell Model of the 400 V IM	33
4.1	Measurements	34
4.2	Simulations	34
4.3	Analytical Calculations	34
5	Result	37
5.1	Identified Induction Machine Circuit Parameters	37
5.1.1	The 400 V IM	37
5.1.2	The 48 V IM	41

5.2	Efficiency Evaluation and Comparison to Circuit Model	45
5.2.1	The 400 V IM	45
5.2.2	The 48 V IM	49
5.3	Efficiency and Torque Comparison between the 48 V IM and the 48 V PMSM	55
5.3.1	Torque and Power Comparison	55
5.3.2	Efficiency Comparison	56
5.3.3	Drive Cycle Analysis Comparison	59
5.4	Sustainability	60
5.4.1	Cost Comparison between IM and PMSM	60
5.4.2	Environmental and Social Comparison	62
6	Discussion	65
7	Conclusion	67
7.1	Future Work	68
	Bibliography	69
A	M700-50A Core Loss Data	I
B	Additional Loss Plots for the 48 V Machines	III

Nomenclature

η	Efficiency [%]
η_{DC}	Drive cycle efficiency [%]
η_{ice}	Average efficiency of the ICE [%]
γ_p	Winding pitch factor
λ_{hew}	Stator end winding height leakage permeance factor
λ_{weu}	Stator end winding width leakage permeance factor
λ_w	Stator end winding leakage permeance factor
μ_0	Vacuum permeability [H/m]
Ω_r	Mechanical rotor frequency [rad/s]
ω_r	Electrical rotor frequency [rad/s]
Ω_s	Synchronous frequency divided with number of pole pairs [rad/s]
ω_s	Synchronous frequency [rad/s]
ρ_{al}	Aluminium resistivity [Ωm]
ρ_{cu}	Copper resistivity [Ωm]
\underline{I}_c	Core loss current phasor [A]
\underline{I}_m	Magnetising current phasor [A]
\underline{I}_r	Rotor current phasor [A]
\underline{I}_s	Stator current phasor [A]
\dot{i}_c	Core loss current space vector [A]
\dot{i}_m	Magnetising current space vector [A]
\dot{i}_r	Rotor current space vector [A]
\dot{i}_s	Stator current space vector [A]
\underline{U}_m	Magnetising voltage phasor [V]
\underline{U}_s	Stator voltage phasor [V]

\underline{u}_s	Stator voltage space vector [V]
A_{cond}	Conductor cross section area [m^2]
$A_{r,slot}$	Rotor bar cross section area [m^2]
A_{scr}	Short circuit ring cross section area [m^2]
c_s	Number of parallel branches
E_{diesel}	Energy content of one litre of diesel [Wh]
$E_{loss,g}$	Total losses during generation [Wh]
$E_{loss,m}$	Total losses during motoring [Wh]
$E_{mech,g}$	Total mechanical energy during generation [Wh]
$E_{mech,m}$	Total mechanical energy during motoring [Wh]
f	Supply frequency [Hz]
h_{ew}	Stator end winding height [m]
h_{gap}	Airgap length [m]
h'_{gap}	Equivalent airgap length with respect to slotting [m]
h_{r0}	Rotor slot opening height [m]
h_{r1}	Rotor slot closing height [m]
h_{r2}	Rotor slot body height [m]
h_{s0}	Stator slot opening height [m]
h_{s1}	Stator slot closing height [m]
h_{s2}	Stator slot body height [m]
I_m	Magnetising current magnitude [A]
I_r	Rotor current magnitude [A]
I_s	Stator current magnitude [A]
$I_{s,max}$	Maximum stator current [A]
i_{sd}	Stator current in d-direction [A]
i_{sq}	Stator current in q-direction [A]
k_1	Winding factor for the fundamental frequency
L_m	Magnetising inductance of the inverse gamma model [H]
L_s	Stator leakage inductance [H]
L_σ	Inverse gamma model leakage inductance [H]
l_a	Active machine length [m]

L_{bar}	Leakage inductance of a single rotor bar [H]
l_{bar}	Rotor bar length [m]
L_{ew}	Stator end winding inductance per phase [H]
l_{ew}	Average length of stator end winding [m]
L_{mT}	T-model magnetising inductance [H]
$L_{r\lambda,r}$	Rotor leakage inductance [H]
$L_{r\lambda}$	T-model rotor leakage inductance [H]
$L_{s\lambda,ew}$	Stator end winding leakage inductance [H]
$L_{s\lambda,slot}$	Stator slot leakage inductance [H]
$L_{s\lambda}$	T-model stator leakage inductance [H]
L_{scr}	Short circuit ring inductance [H]
l_s	Equivalent length of stator [m]
n	Rotor speed [rpm]
n_{max}	Maximum rotor speed [rpm]
N_{ph}	Number of phases
n_p	Number of pole pairs
n_s	Number of stator turns per slot
p	Number of poles
p_v	Impedance transformation factor from rotor to stator
P_{airgap}	Airgap power [W]
P_c	Core losses [W]
$P_{loss,dq}$	Total losses from the dq circuit model [W]
P_{loss}	Total losses [W]
P_{mech}	Mechanical power [W]
$P_{r,stray}$	No load stray losses in the rotor bars [W]
P_{rb}	Rotor bar losses [W]
P_{sw}	Stator winding losses [W]
Q	Reactive power [VAr]
Q_r	Number of rotor bars
Q_s	Number of stator slots
q_s	Number of slots per pole per phase

R_r	Rotor resistance of the inverse gamma model [Ω]
r_r	Rotor radius [m]
R_s	Stator resistance [Ω]
R_{bar}	Resistance of a single rotor bar [Ω]
R_c	Core loss resistance [Ω]
R_d	d-axis resistance [Ω]
r_{fill}	Stator slot fillet radius [m]
R_q	q-axis resistance [Ω]
$R_{r,r}$	Rotor resistance [Ω]
R_{rT}	T-model rotor resistance [Ω]
$r_{s,out}$	Stator outer radius [m]
R_{scr}	Short circuit ring resistance [Ω]
r_{scr}	Short circuit average ring radius [m]
R_{sew}	Stator end winding resistance [Ω]
r_{shaft}	Shaft radius [m]
s	Slip of the IM
T	Electromagnetic torque [Nm]
T_{max}	Maximum electromagnetic torque [Nm]
T_{sim}	Simulated electromagnetic torque [Nm]
U_m	Magnetising voltage magnitude [V]
U_s	Stator voltage magnitude [V]
U_{DC}	DC-link voltage [V]
U_{LL}	Line to line voltage [V]
$U_{s,max}$	Maximum stator voltage [V]
u_{sd}	Stator voltage in d-direction [V]
u_{sq}	Stator voltage in q-direction [V]
w_{ew}	Stator end winding width [m]
w_{r0}	Rotor slot opening width [m]
w_{r1}	Rotor slot outer width [m]
w_{r2}	Rotor slot inner width [m]
w_{s0}	Stator slot opening width [m]

w_{s1} Stator slot inner width [m]

w_{s2} Stator slot outer width [m]

Acronyms

FEM Finite Element Method

GWP Global Warming Potential

ICE Internal Combustion Engine

IM Induction Machine

IM_{Cu} Induction Machine with copper rotor bars

NdFeB Neodymium Iron Boron

PMSM Permanent Magnet Synchronous Machine

1

Introduction

Today electrification within the vehicle industry is developing at a rapid pace to meet society's demand of cleaner and more sustainable transportation. The most commonly used electric machine within the industry is the Neodymium Iron Boron (NdFeB) PMSM, because of its high efficiency and high torque performance. However, the IM could provide a cheap and sustainable alternative to the PMSM. The IM uses only metal bars in the rotor and has no need for permanent magnets, that are both more expensive and less environmentally friendly. Additionally, in literature there are lacking relevant comparisons between the performance of the PMSM and the IM in vehicle applications.

This thesis compares the efficiency and torque performance of the two machines, as well as their sustainability. The focus of the thesis work is put on the IM, since the PMSM is already well documented in literature. A hardware design of a 48 V IM for mild hybrid application is developed in a FEM software and its efficiency is evaluated with a minimum loss control. The IM is then compared with a 48 V PMSM developed by [1].

1.1 Background

One of the reasons for the electrification of vehicles is the need of reduced greenhouse gas emissions. In 2016 the road transport was responsible for 21 % of the CO₂ emissions in the EU [2]. The European commission has set up a target of reducing the average emissions of new cars to 95 g CO₂/km from 2021 [3]. They have also implemented a strategy to move towards zero-emission vehicles [2]. The mild hybrid has been a way of electrifying cars that are still using an Internal Combustion Engine (ICE) as the main propulsion motor. The mild hybrid uses a smaller electric machine in addition to the ICE to save fuel and increase the overall efficiency of the vehicle [4], thereby emissions are reduced. Although, the most commonly used electric machine is the PMSM, which is still connected with social and environmental impacts. This is mainly due to the usage of NdFeB permanent magnets [5, 6, 7, 8]. From an economical perspective, the essential constituents Dy and Nd of the permanent magnets are also considered a supply risk, due to previous price fluctuations and the fact that China controls 90 % of the production of rare earth metals [9, 10, 11].

Therefore it would be of great interest to investigate how the IM would compare to a PMSM in a mild hybrid application, since the IM has no need for permanent magnets.

1.2 Aim

There are two main aims of this master's thesis. The first aim is to develop a steady state minimum loss control algorithm for an IM. The second aim is to design a 48 V IM and compare its suitability for mild hybrid applications with a previously developed NdFeB PMSM of the same volume. The comparison is done in terms of efficiency, torque performance, cost and sustainability.

1.3 Problem Definition

First and foremost, possible ways to represent the IM as a circuit model need to be evaluated. The model is used as a tool to develop the steady state minimum loss control algorithm of the machine. The circuit model should be able to account for as many losses as possible in the actual machine, at the same time as it provides enough simplicity for control calculations. A typical control approach is to use an inverse gamma model [12]. However, the core and stray losses of the IM cannot be neglected since they account for a considerable part of the losses to be minimised. Therefore another suitable circuit model must be found.

Further on, a method for identifying the parameters of the circuit model from the actual geometry of the machine must be established. The primary tool for this problem is the FEM software Ansys Maxwell. The software is used to model the machine geometry, as well as simulate current and frequency dependencies of the desired circuit model parameters. At the beginning of the thesis work an already available Maxwell model of a 400 V IM is used. This grants the opportunity of directly starting to develop the control algorithm, without first building a new machine model in the FEM software.

Once the steady state minimum loss control algorithm is developed, the 48 V IM for mild hybrid applications is designed in Ansys Maxwell. A method for setting up an initial geometry must be investigated and then followed by parameter sweeps in the FEM software to find an improved design. The 48 V IM is compared with a previously developed 48 V PMSM, to conclude its suitability for mild hybrids. The result is to be presented in efficiency maps and maximum torque lines, so that the difference between the two machines at different operating points is clearly shown.

Finally, the 48 V IM and the 48 V PMSM are compared in the terms of sustainability. The cost and supply risks of the materials in each machine need to be investigated, as well as the social and environmental impacts connected to the extraction of the machine materials.

1.4 Scope

The circuit model of the IM used for the steady state minimum loss control algorithm takes into account I^2R -losses in stator windings and rotor bars, core losses and the no load stray loss called *tooth flux pulsation cage circulating current loss*, further explained in section 2.4. No other stray losses are taken into account in order to keep the circuit model complexity at a reasonable level. Mechanical losses are also disregarded since the thesis focuses on electrical aspects.

The minimum loss algorithm only controls the steady state reference of the IM. Thereby no transients are taken into account in the efficiency evaluation of the machines. The efficiency also only takes the electric machine in consideration. The losses in the inverter, battery and cables are disregarded.

The design of the 48 V IM focuses only on electromagnetic design in Ansys Maxwell. No thermal analysis is done. Cutting and welding effects on core losses during manufacturing are also disregarded.

2

Three Phase Induction Machine Theory

The three phase induction machine is a cheap, robust and reliable electric machine [13]. This has made it widely used in industrial applications. A cutaway model of a typical IM can be seen in figure 2.1. The IM includes a rotor (1) made of laminated steel with aluminium or copper bars inside and a short circuit ring (2) connecting these bars. A shaft (3) transfers the rotational power to the load. Around the rotor is a stator, containing a core of laminated steel and a copper winding (4), (5). The active part of the copper winding (4) is inside the stator core while the end winding (5) is located outside the core. All of this is enclosed in a case protecting the machine.



Figure 2.1: Cutaway model of an induction machine. 1) Rotor 2) Slip ring 3) Shaft 4) Active part of stator winding 5) Stator end winding. Adapted from [14]. Public domain.

2.1 T-model and Analytic Parameter Estimation of the IM

The three phase induction machine, depicted in figure 2.1 can be represented as an electric circuit model for each phase. The most common model for this purpose is the T-model presented in figure 2.2.

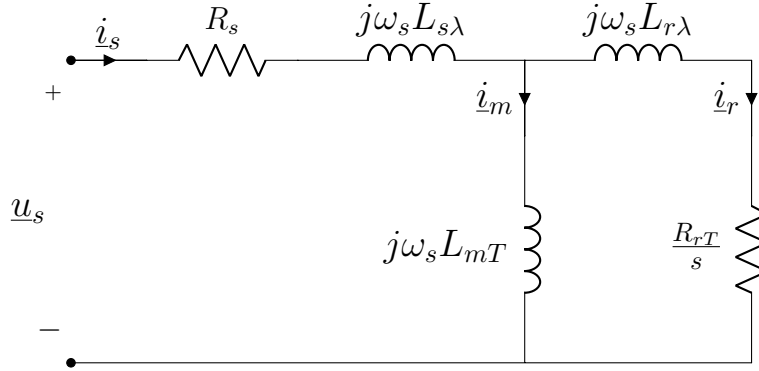


Figure 2.2: T-model of the IM

A rough estimation of the circuit parameters can be made by using analytic calculations based on the IM's geometry. The following method for determining these parameters is taken from [15], which in turn is based on [16].

The stator winding resistance per phase, R_s , is calculated as

$$R_s = \frac{2q_s n_s \rho_{cu} (l_{ew} + l_a)}{c_s A_{cond}}, \quad (2.1)$$

where q_s is the number of slots per pole per phase, n_s is the number of turns per slot, c_s is the number of parallel branches, A_{cond} is the conductor cross section area, ρ_{cu} the resistivity of copper, l_{ew} is the average length of an end winding segment and l_a is the active length of stator winding.

The stator winding leakage inductance $L_{s\lambda}$ is determined as the sum of the stator slot leakage inductance and the end winding leakage inductance. The stator slot leakage inductance $L_{s\lambda,slot}$ is calculated as

$$L_{s\lambda,slot} = \frac{\mu_0 p n_s^2 q_s^2 l_a}{3c_s^2} \left(\frac{2(h_{s1} + h_{s2} + r_{fill})}{w_{s1} + w_{s2}} + \frac{3h_{s0}}{w_{s0}} \right), \quad (2.2)$$

where h_{s0} , h_{s1} , h_{s2} , w_{s0} , w_{s1} , w_{s2} , r_{fill} are geometric parameters for the stator slot shown in figure 3.1, p is the number of poles and μ_0 is the vacuum permeability. The end winding leakage inductance $L_{s\lambda,ew}$ is calculated as

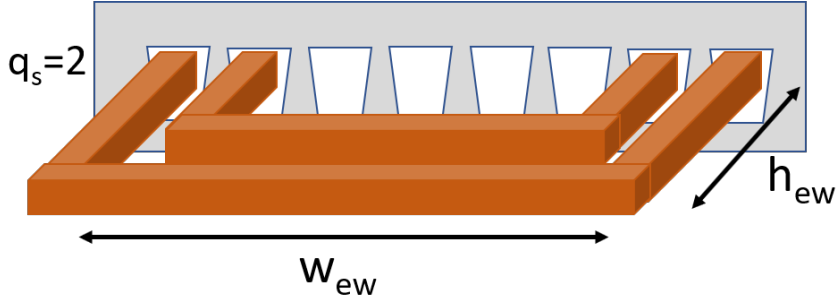


Figure 2.3: Stator end winding height and width.

$$L_{s\lambda,ew} = \frac{Q_s}{N_{ph}} q_s \left(\frac{n_s}{c_s} \right)^2 \mu_0 l_{ew} \lambda_w, \quad (2.3)$$

where Q_s is number of stator slots, N_{ph} the number of phases and

$$l_{ew} \lambda_w = 2h_{ew} \lambda_{hew} + w_{ew} \lambda_{wew}. \quad (2.4)$$

l_{ew} and w_{ew} are the average length and width of the end winding which are illustrated in figure 2.3. $\lambda_{l_{ew}}$ and $\lambda_{w_{ew}}$ are empirically determined permeance factors which can be found in [16].

Adding (2.2) and (2.3) yields $L_{s\lambda}$ as

$$L_{s\lambda} = L_{s\lambda,slot} + L_{s\lambda,ew}. \quad (2.5)$$

The magnetising inductance L_{mT} is calculated as

$$L_{mT} = \frac{6\mu_0 n_s^2 q_s^2 k_1^2 l_a r_r}{\pi c_s^2 h'_{gap}}, \quad (2.6)$$

where r_r is the rotor radius, h'_{gap} is an equivalent air gap length with respect to slotting and k_1 is the winding factor for the fundamental frequency calculated as

$$k_1 = \frac{\sin(\frac{\pi}{6})}{q_s \sin(\frac{\pi}{6q_s})} \cos(\frac{\gamma_p p}{2}), \quad (2.7)$$

where γ_p is the winding pitch factor.

The rotor resistance and inductance is determined by two parts in the rotor, the rotor bars and the short circuit ring. The resistance of a single rotor bar R_{bar} is

calculated as

$$R_{bar} = \frac{\rho_{al} l_a}{A_{r,slot}}, \quad (2.8)$$

where $A_{r,slot}$ is the area of a rotor slot. The resistance of a short circuit segment R_{scr} is calculated as

$$R_{scr} = \frac{2\pi\rho_{al}r_{scr}}{Q_r A_{scr}}, \quad (2.9)$$

where Q_r is the number of rotor bars, r_{scr} is the average radius of the short circuit ring and A_{scr} is the cross section of the short circuit ring. The leakage inductance of a single rotor bar L_{bar} is calculated as

$$L_{bar} = \frac{\mu_0 n_s^2 q_s^2 p^2 l_a}{Q_r c_s^2} \frac{(h_{r0} + h_{r1} + h_{r2})^2}{w_{r0} h_{r0} + 0.5(w_{r1} + w_{r0}) h_{r1} + 0.5(w_{r1} + w_{r2}) h_{r2}} \quad (2.10)$$

where h_{r0} , h_{r1} , h_{r2} , w_{r0} , w_{r1} and w_{r2} are geometric parameters of the rotor bar, shown in figure 3.1. The leakage inductance of a short circuit segment L_{scr} is calculated as

$$L_{scr} = \frac{\mu_0 Q_r}{N_{ph} n_p^2} \frac{1}{3} \left[(l_{bar} - l_s) + 0.18 \frac{2\pi r_{scr}}{2n_p} \right], \quad (2.11)$$

where n_p number of pole pairs, l_{bar} is the rotor bar length and l_s is the equivalent length of the stator.

Since the current through the rotor bar and the short circuit ring is not equal, the total rotor resistance/inductance can not be found by simply adding R_{bar}/L_{bar} and R_{scr}/L_{scr} . Instead the total rotor resistance $R_{r,r}$ can be calculated as

$$R_{r,r} = R_{bar} + 2R_{scr} \left(\frac{Q_r}{\pi p} \right)^2. \quad (2.12)$$

Similarly the rotor leakage inductance $L_{r\lambda,r}$ is calculated as

$$L_{r\lambda,r} = L_{bar} + 2L_{scr} \left(\frac{Q_r}{\pi p} \right)^2. \quad (2.13)$$

$R_{r,r}$ and $L_{r\lambda,r}$ are then transformed to stator quantities by multiplying them with the factor

$$p_v = \frac{N_{ph} n_s^2 q_s^2 k_1^2 p^2}{Q_r c_s^2}, \quad (2.14)$$

yielding the rotor resistance transformed to the stator side R_{rT} as

$$R_{rT} = p_v R_{r,r} \quad (2.15)$$

and the rotor leakage inductance transferred to the stator side $L_{r\lambda}$ as

$$L_{r\lambda} = p_v L_{r\lambda,r}. \quad (2.16)$$

2.2 Inverse Gamma Model with Core Losses

For control applications the T-model is often simplified to reduce the complexity of the control system. One simplified model is the inverse gamma model which can be derived from the T-model by transforming the model such that the rotor leakage inductance becomes zero [17]. The inverse gamma model only accounts for resistive losses in the stator winding and in the rotor bars. To also account for the core losses, a resistor R_c , is added in parallel to the magnetising inductance [18]. The inverse gamma model in steady state with R_c added is shown in figure 2.4.

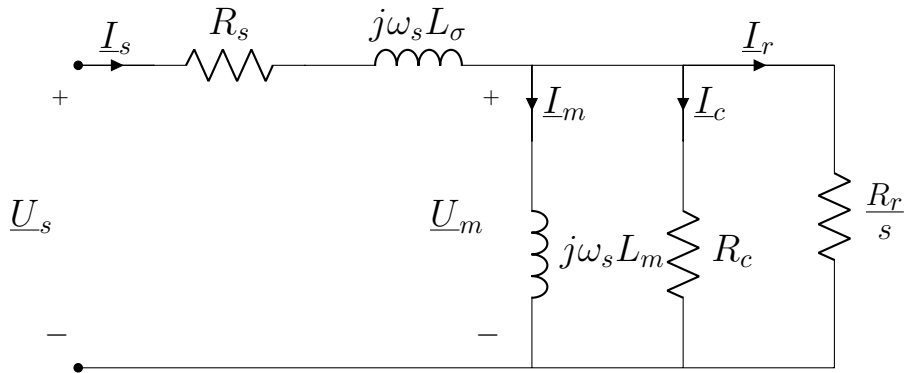


Figure 2.4: Steady state inverse gamma model with added core loss resistance

The current and voltages in figure 2.4 are transformed to dq-quantities using amplitude invariant transformation. The dq-quantities are used for simplification of control calculations. Perfect field orientation is assumed, meaning that the d-axis is aligned with the magnetising current i_m , such that $i_m = i_{sd}$ and $i_{sq} = i_c + i_r$. The equivalent rotor resistance $\frac{R_r}{s}$ is divided into the loss component and the back emf voltage. The model with dq-quantities can be seen in figure 2.5.

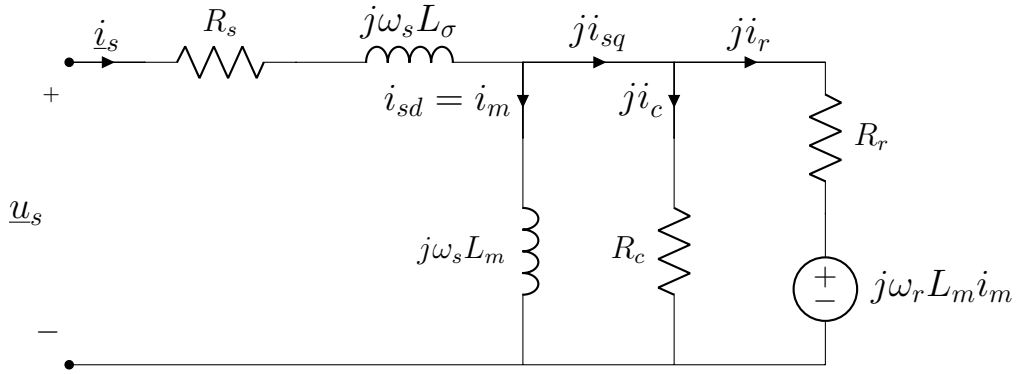


Figure 2.5: Inverse gamma model with added core loss resistance in dq-quantities

Using figure 2.5, the stator current and voltage are expressed as

$$\underline{i}_s = i_{sd} + j i_{sq} \quad (2.17)$$

and

$$\underline{u}_s = u_{sd} + j u_{sq}, \quad (2.18)$$

where

$$u_{sd} = R_s i_{sd} - \omega_s L_\sigma i_{sq} \quad (2.19)$$

$$u_{sq} = R_s i_{sq} + \omega_s L_\sigma i_{sd} + \omega_s L_m i_{sd} \quad (2.20)$$

The torque produced by the IM is calculated from the mechanical power P_{mech} and rotor frequency Ω_r as

$$T = \frac{P_{mech}}{\Omega_r} = \frac{3}{2} n_p L_m i_d i_r. \quad (2.21)$$

It is also possible to express the torque as a function of the air gap power, P_{airgap} instead of the mechanical power. Then the torque expression becomes

$$T = \frac{P_{airgap}}{\Omega_s}, \quad (2.22)$$

since $P_{mech} = P_{airgap}(1 - s)$ and $\Omega_r = \Omega_s(1 - s)$. The feeding frequency ω_s of the machine can be derived from figure 2.5 as

$$\omega_s = \omega_r + \frac{R_r i_r}{L_m i_{sd}}. \quad (2.23)$$

2.3 Circuit Model Losses

The inverse gamma model with core losses in figure 2.5 includes three loss components represented by the three resistors R_s , R_r and R_c . The Stator winding resistance is represented by R_s which causes resistive losses P_{sw} . The rotor bar resistance is represented by R_r which causes resistive losses, P_{rb} . The resistance causing eddy current and hysteresis losses in the electrical steel P_{core} is represented by R_c . From figure 2.5, the three loss components are expressed as

$$P_{loss} = P_{sw} + P_{rb} + P_{core} = R_s(i_{sd}^2 + i_{sq}^2) + R_r i_r^2 + R_c(i_{sq}^2 - i_r^2). \quad (2.24)$$

In order to apply (2.24) in a control algorithm, (2.24) is rewritten in terms of the control input parameters i_{sd} , i_{sq} and ω_r by rewriting i_r from the relation of the q-axis current in figure 2.5

$$i_{sq} = i_r + i_f = i_r + \frac{\omega_r L_m i_{sd} + i_r R_r}{R_c},$$

as

$$i_r = \frac{R_c}{R_c + R_r} i_{sq} - \omega_r \frac{L_m}{R_c + R_r} i_{sd}. \quad (2.25)$$

Inserting (2.25) into (2.24) yields

$$P_{loss,dq} = R_d i_{sd}^2 + R_q i_{sq}^2, \quad (2.26)$$

where

$$R_d = R_s + \frac{L_m^2}{R_m + R_r} \omega_r^2, \quad R_q = R_s + \frac{R_m R_r}{R_m + R_r}. \quad (2.27)$$

2.4 Stray Losses in Rotor Bars

Additional losses in the stator and rotor geometry caused by space harmonics are usually referred to as stray losses. A total of thirteen different kinds of stray losses for induction machines with frequency application above 50-60 Hz are described by [19]. These losses can be divided into no-load stray losses and load stray losses. However, in this thesis only the no-load stray loss affecting the rotor bars is taken into account, as mentioned in the scope. This loss is called *tooth flux pulsation cage circulating current loss*. It is one of the more considerable stray losses and it increases rapidly with increase of supply frequency. The loss originates from ripples in the air gap flux due to permeance variations in the magnetic flux path when

the relative positions of the rotor teeth and the stator slots change with rotation, which is displayed in figure 2.6 and 2.7. When the rotor teeth are right above the stator teeth the permeance of the flux path is high, resulting in a high magnetic flux density in the air gap as in figure 2.6. When the rotor teeth are right above the stator slot on the other hand, the permeance of the magnetic flux path is low. This causes the magnetic flux density in the air gap to reduce, as can be seen in figure 2.7. The constant change in relative position between the rotor and stator teeth causes magnetic flux ripples that induce harmonic currents in the rotor cage and generate additional RI^2 -losses [19].

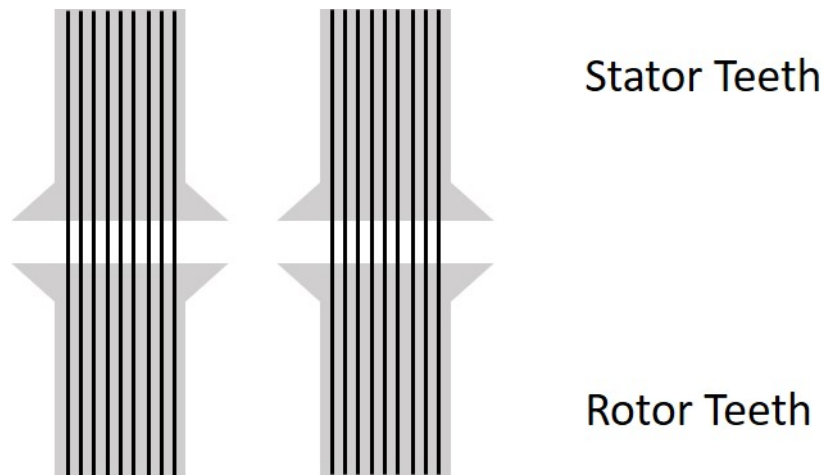


Figure 2.6: High permeance flux path.

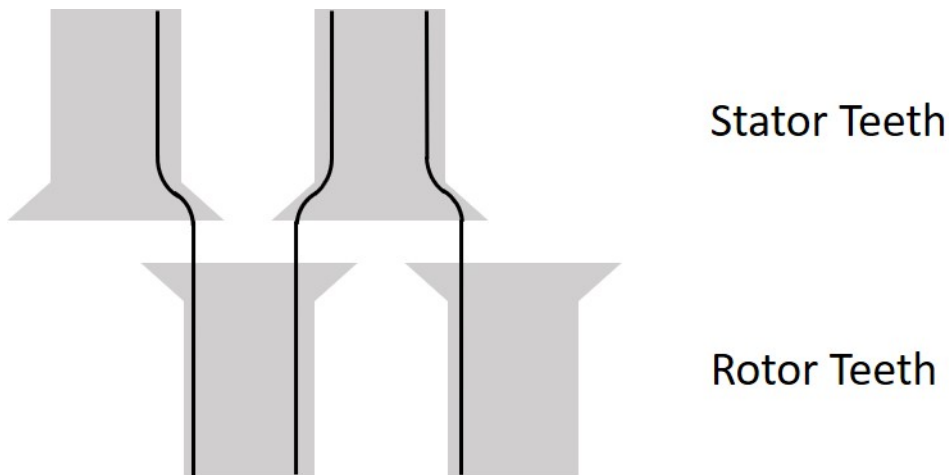


Figure 2.7: Low permeance flux path.

3

Case Set-up

This chapter presents the overall resources and methodology used to evaluate the induction machines and the permanent magnet machine that are considered in this thesis. The electric machines were mainly evaluated using the FEM software Ansys Maxwell, since it allowed to solve for the electromagnetic fields in the complex geometries of the electric machines in a more precise manner than an analytical approach could provide. Additionally, Matlab was used to develop the steady state control algorithm with data provided from the FEM software. Overall drive cycle efficiencies for the electric machines were also determined with existing data from two drive cycles in Gothenburg. The sustainability of the machines was evaluated with a literature study.

3.1 Simulation Set-up in Ansys Maxwell

In order to evaluate the electric machines the FEM-software Ansys Maxwell was used. All simulations were done according to the assumptions below.

- All models were made in 2D to save computational time.
- The solution type Magnetic Transient was used since the problem involved time varying magnetic fields.
- All simulations were done using sinusoidal voltage feeding if nothing else is stated.
- The stator windings were set as a stranded object, meaning that no eddy currents existed in the windings. This saved computational time and was a good approximation when the number of strands was high.
- The rotor bars were set as a solid object, meaning eddy currents were induced. This was necessary for the torque production in the rotor.
- The core material was M700-50A in both the 400 V IM and the 48 V IM. The core losses connected to the material are presented in figure A.1 in appendix

A.

- The stator resistance and the stator end winding inductance were calculated manually according to (2.1) and (2.3). These parameters were used as input data to Maxwell to include the most important end effects of the stator.
- The resistance and the inductance of the short circuit ring segment were calculated manually according to (2.9) and (2.11), and set as an end connection for the rotor bars in Maxwell. This was done to include the most important end effects of the rotor.
- Axial symmetry was used to reduce the models to the smallest size, in order to save computational time.

3.2 Electric Machine Models

There were three Maxwell models of electric machines involved in this thesis. The first machine model was a 400 V IM created by Torbjörn Thiringer [20], that was used to develop the steady state minimum loss control algorithm. The second machine model was a 48 V IM that was designed in this thesis work from an initial geometry presented by [21, 15]. The 48 V IM design and performance evaluation were done with aluminium rotor bars. The final design was also evaluated with copper as rotor bars, but the machine is then specifically referred to as the Induction Machine with copper rotor bars (IM_{Cu}). The parameters used to describe the geometry of the induction machines are defined according to the layout in figure 3.1. Finally, the third machine model was an 8-pole 48 V PMSM originally created by Sebastian Larqvist and Hannes Östergren during their master's thesis work [1]. This machine model was used as a comparison to the 48 V IM.

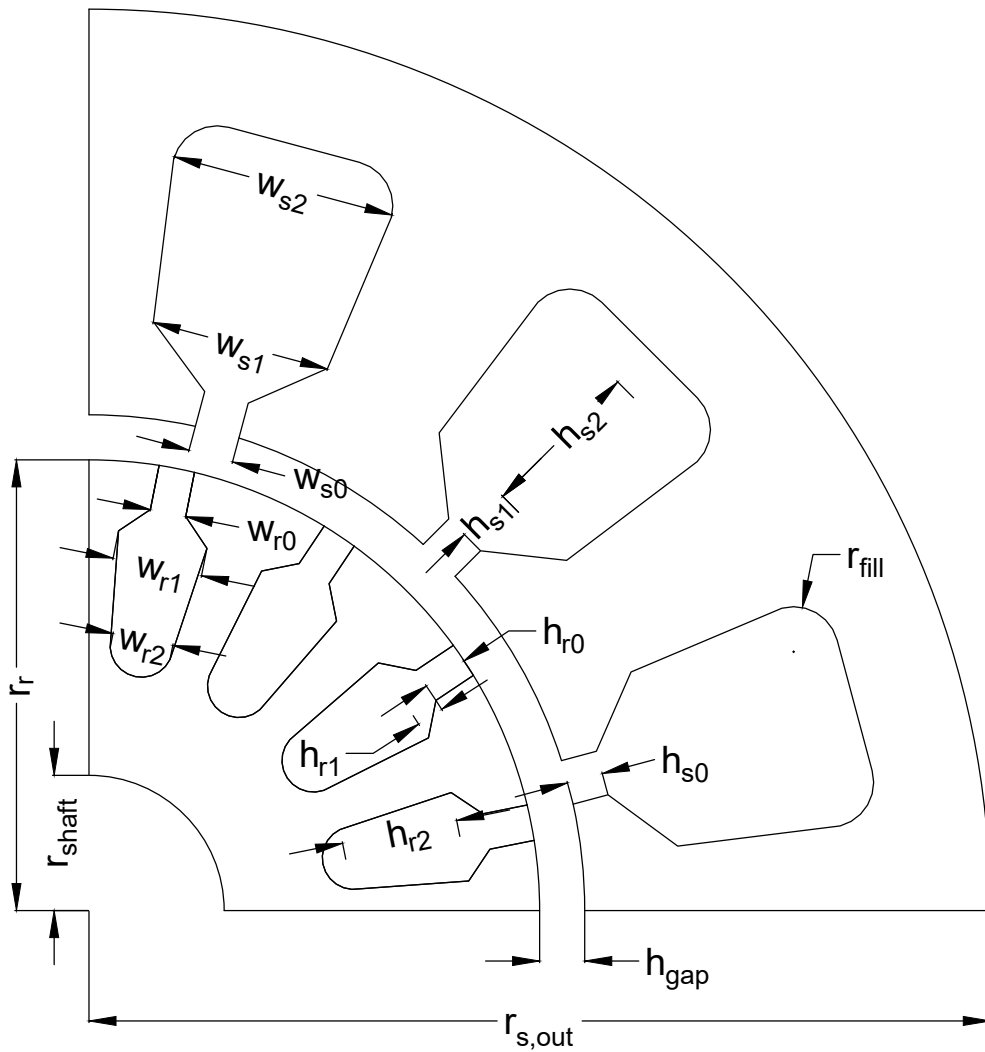


Figure 3.1: Geometrical parameters of the induction machines

3.2.1 The 400 V IM Model

The Maxwell model of the 400 V IM was already available at the start of the thesis work [20] and was therefore used to develop the steady state minimum loss control algorithm. It was designed after a real machine used for industrial applications. The parameter values are presented in table 3.1. As mentioned, the definition of each geometric parameter is visualised in figure 3.1. The geometry and the mesh of the machine model are shown in figure 3.2.

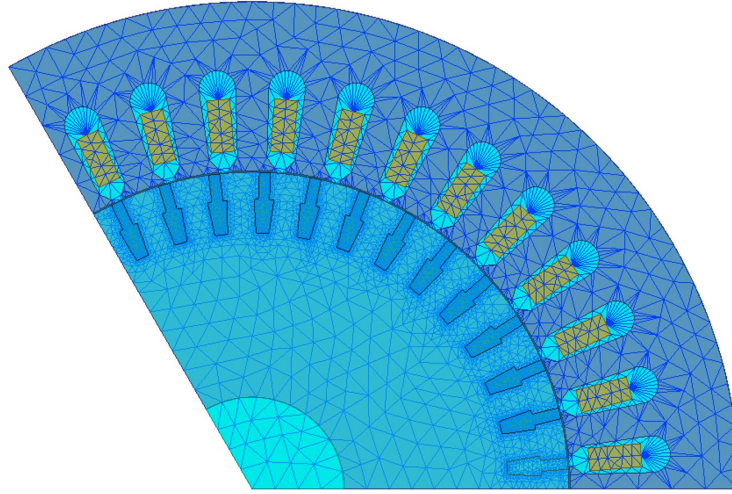


Figure 3.2: Maxwell model geometry and mesh for the 400 V IM. The number of elements in the mesh were 10 312.

Table 3.1: Machine parameters for the 400 V IM

Parameter	Description	Value
p	Poles	6
N_{ph}	Phases	3
c_s	Parallel branches	2
q_s	Slots per pole per phase	2
n_s	Turns per slot	38
Q_s	Stator slot number	36
Q_r	Rotor slot number	39
l_a	Active length	230.00 mm
$r_{s,out}$	Stator outer radius	145.60 mm
r_r	Rotor radius	94.65 mm
r_{shaft}	Shaft radius	27.50 mm
r_{fill}	Stator slot fillet radius	5.50 mm
h_{gap}	Airgap length	0.45 mm
h_{s0}	Stator slot opening height	1.00 mm
h_{s1}	Stator slot closing height	3.00 mm
h_{s2}	Stator slot body height	20.85 mm
w_{s0}	Stator slot opening width	3.50 mm
w_{s1}	Stator slot inner width	8.50 mm
w_{s2}	Stator slot outer width	11.00 mm
h_{r0}	Rotor slot opening height	8.00 mm
h_{r1}	Rotor slot closing height	2.00 mm
h_{r2}	Rotor slot body height	11.00 mm
w_{r0}	Rotor slot opening width	3.35 mm
w_{r1}	Rotor slot outer width	5.90 mm
w_{r2}	Rotor slot inner width	3.90 mm
$I_{s,max}$	Maximum stator current	32 A
R_{scr}	Short circuit ring resistance	1.03 $\mu\Omega$
L_{scr}	Short circuit ring inductance	36 nH
R_s	Stator winding phase resistance	0.184 Ω

3.2.2 The 48 V IM Model - Design Procedure

The final design of the 48 V IM is presented in figure 3.3 and its parameters in table 3.2. All geometrical parameters are also visualised in figure 3.1.

Table 3.2: Parameters of the final geometry of the 48 V IM.

Parameter	Description	Value
p	Poles	4
N_{ph}	Phases	3
c_s	Parallel branches	2
q_s	Slots per pole per phase	2
n_s	Turns per slot	8
Q_s	Stator slots	24
Q_r	Rotor slots	32
l_a	Active length	80.00 mm
l_{ew}	Stator end winding length	138.00 mm
$r_{s,out}$	Stator outer radius	82.50 mm
r_r	Rotor radius	51.00 mm
r_{shaft}	Shaft radius	20.00 mm
r_{fill}	Stator slot fillet radius	1.00 mm
h_{gap}	Airgap length	0.50 mm
h_{s0}	Stator slot opening height	0.50 mm
h_{s1}	Stator slot closing height	2.00 mm
h_{s2}	Stator slot body height	13.80 mm
w_{s0}	Stator slot opening width	6.00 mm
w_{s1}	Stator slot inner width	8.10 mm
w_{s2}	Stator slot outer width	11.80 mm
h_{r0}	Rotor slot opening height	0.50 mm
h_{r1}	Rotor slot closing height	3.00 mm
h_{r2}	Rotor slot body height	12.00 mm
w_{r0}	Rotor slot opening width	2.50 mm
w_{r1}	Rotor slot outer width	5.50 mm
w_{r2}	Rotor slot inner width	3.14 mm
$I_{s,max}$	Maximum stator current	283 A
R_{scr}	Short circuit ring resistance	0.84 $\mu\Omega$
L_{scr}	Short circuit ring inductance	14 nH
R_s	Stator winding phase resistance	6.7 $m\Omega$
L_{ew}	Stator end winding inductance	11.7 μH .
n_{max}	Maximum rotor speed	16 000 rpm

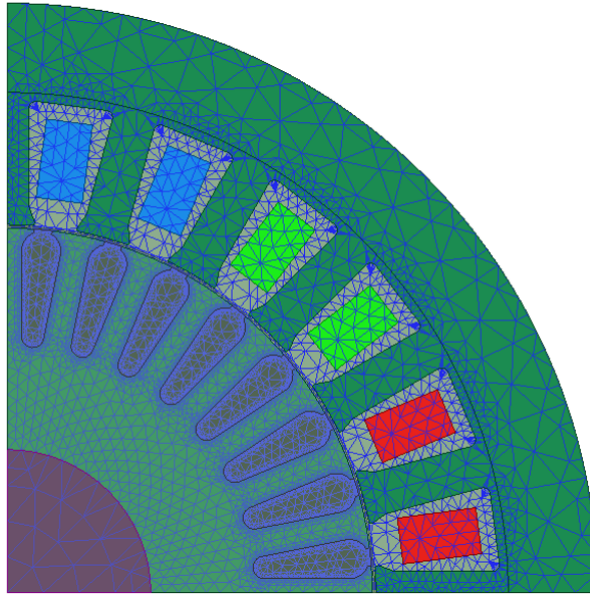


Figure 3.3: Final design of the 48 V IM geometry. The mesh contains 13 384 elements.

The 48 V IM was given the same active volume as the 48 V PMSM designed by [1], to make a relevant comparison of the two machines. Therefore the stator outer radius was set to 82.5 mm, the active length to 80 mm. The 48 V IM was then designed by using a method for determining an initial geometry presented by [21]. The parameter values of the initial geometry that were evaluated before being included in the final geometry are presented in table 3.3. The stator resistance R_s used in the design was calculated according to (2.1),

$$R_s = 6.7 \text{ m}\Omega,$$

where the cross section area of the copper wire A_{cond} was 8.75 mm^2 .

Table 3.3: Parameters of the initial geometry of the 48 V IM.

Parameter	Description	Initial value
h_{s0}	Stator slot opening height	1.00 mm
h_{r0}	Rotor slot opening height	0.50 mm
h_{r1}	Rotor slot closing height	3.00 mm
h_{r2}	Rotor slot body height	12.40 mm
w_{s0}	Stator slot opening width	3.00 mm
w_{r0}	Rotor slot opening width	0.50 mm
w_{r2}	Rotor slot inner width	2.20 mm

Further on, FEM-analysis in Ansys Maxwell was used to sweep different parameters in the initial geometry to give an improved design. In mild hybrid applications an

important function is to use the electric machine for cranking, meaning that the electric machine helps the combustion engine to start [4]. Thereby it was of interest to evaluate the performance of the induction machine at high torque and low speed. The electric machine in a mild hybrid application is also used for regeneration of power at braking and for boosting the torque of the vehicle. The efficiency at a lower torque in high speed is therefore also important. To take these functions into account while designing the geometry of the machine, parametric sweeps were done at three operating points:

1. 250 rpm at maximum torque (55 Nm)
2. 4600 rpm and 1.5 to 3 Nm at boosting
3. 4600 rpm and -2 to -3.5 Nm at regeneration

The change of geometric parameter values during the sweep slightly changed the torque the machine was providing, therefore the torque is stated within a range.

Operating Point 1 - Cranking

The first parametric sweep was done at cranking at 250 rpm with 7 V sinusoidal voltage feeding and 12 Hz supply frequency. The same sweep was also done during a locked rotor simulation at 66.67 Hz and 6 V sinusoidal voltage feeding to evaluate the leakage inductance L_σ . The aim of the sweeps were to find a geometry that would minimise the torque ripple and at the same time keep the leakage inductance low to not worsen the high speed performance [22]. The swept parameters were w_{r0} , h_{r0} , w_{s0} and h_{s0} , since these were connected to the leakage inductance [15]. The minimum value of the stator slot opening w_{s0} was set to 2 mm to allow the strands to fit through the opening. The minimum value of the rest of the parameters were set to 0.5 mm to make the design reasonable for manufacturing. One parameter was swept at a time while the rest were kept according to the initial geometry. The resulting peak to peak torque ripple and leakage inductance are presented in figure 3.4.

3. Case Set-up

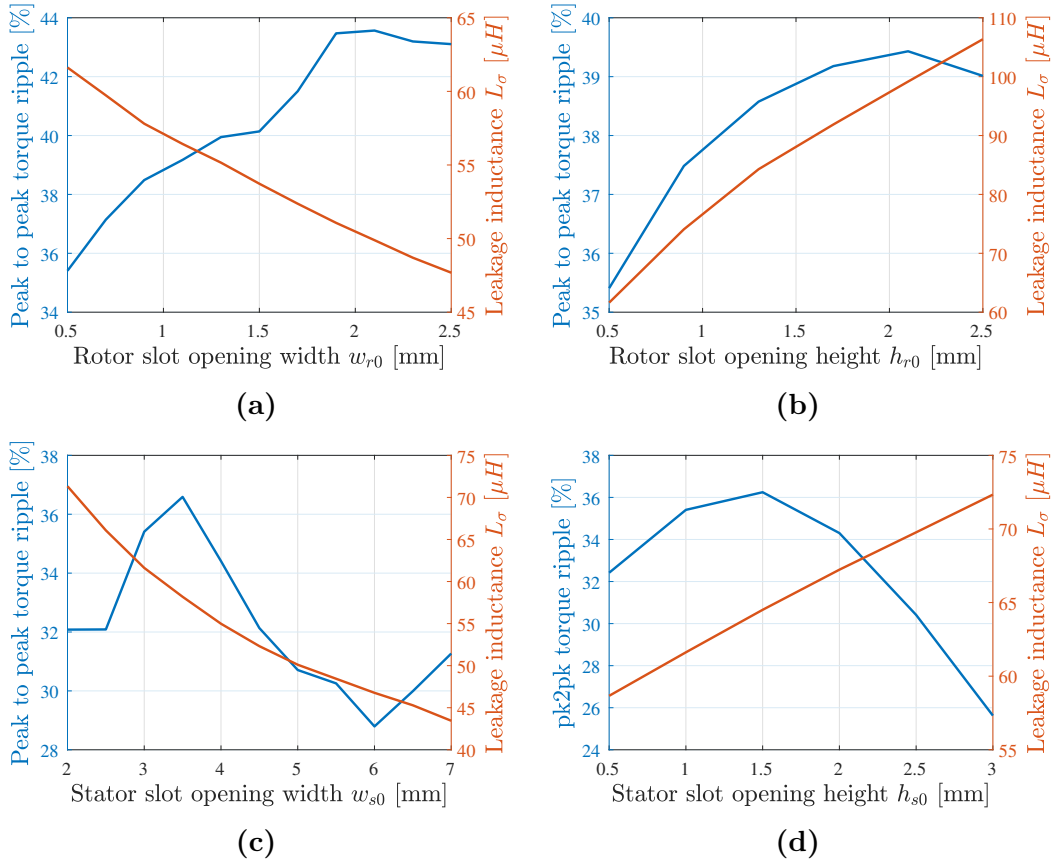


Figure 3.4: Peak-to-peak torque ripple and leakage inductance for slot opening variations. The leakage inductance was calculated from a locked rotor test at 66.67 Hz and 6 V. The torque ripple was calculated at 250 rpm, 7 V and 12 Hz feeding frequency.

From figures 3.4b and 3.4d it can be seen that a lower value of the slot opening heights gives both lower leakage inductance and lower torque ripple. Therefore these parameters were chosen at their lowest value as

$$h_{r0} = 0.5 \text{ mm},$$

$$h_{s0} = 0.5 \text{ mm}.$$

The rotor slot opening width w_{r0} had an opposite correlation to the leakage inductance compared to the torque ripple, as can be seen in figure 3.4a. The opening width was then chosen to the largest investigated value,

$$w_{r0} = 2.5 \text{ mm},$$

to ensure a lower leakage inductance and not compromise the high speed perfor-

mance of the induction machine. Although, this choice came at the cost of higher torque ripple. The result for the stator slot opening width w_{s0} is shown in figure 3.4c. The parameter was chosen as

$$w_{s0} = 6.0 \text{ mm},$$

since it gave the best compromise between leakage inductance and torque ripple.

Operating Point 2 - Boosting

The second sweep was done at 4600 rpm and 1.5 to 3 Nm with sinusoidal voltage feeding. The aim of the sweep was to improve the efficiency of the 48 V IM at this operating point. The varied parameters were the rotor slot body height h_{r2} , the rotor slot outer width w_{r1} and the rotor slot inner width w_{r2} . The relation between w_{r1} and w_{r2} was also adjusted so that the rotor teeth would have an even width. The voltage amplitude and the supply frequency were also adjusted during the sweep so that the 48 V IM would provide torque within the stated range for the different geometries. Four combinations of h_{r2} , w_{r2} and w_{r1} giving high efficiency at operating point 2 are presented in table 3.4, together with the combination of the initial geometry (Combination 5). These combinations were also rerun for operating point 1 at cranking, to ensure that the leakage inductance or torque ripple had not worsened due to the efficiency optimisation of the geometry. Additionally, the maximum torque that the 48 V IM could provide at 250 rpm was evaluated for the five chosen geometries. The result of the rerun of operating point 1 is presented in table 3.5.

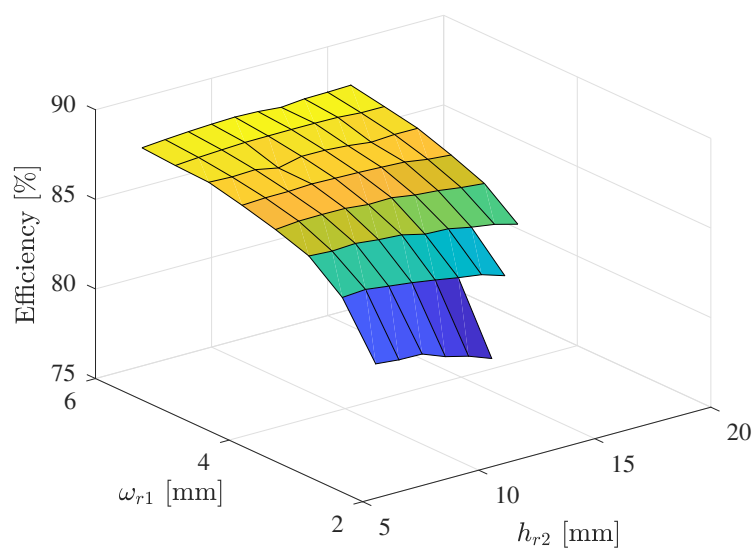


Figure 3.5: Motor efficiency at 2 Nm and 4600 rpm for variations in h_{r2} and ω_{r1} .

Table 3.4: Efficiency at operating point 2 for the five combinations of rotor slot parameters. The combinations are defined by the values of h_{r2} , w_{r1} and w_{r2} .

Geometry	h_{r2} [mm]	w_{r1} [mm]	w_{r2} [mm]	Efficiency [%]
Combination 1	11.0	6.0	3.82	86.8
Combination 2	12.0	5.5	3.14	86.8
Combination 3	12.4	4.6	2.20	86.4
Combination 4	13.0	5.5	2.95	86.4
Combination 5	16.0	6.0	3.86	87.0

Table 3.5: Rerun of operating point 1 for the five combination of rotor slot parameters.

Geometry	Torque ripple [%]	Maximum torque [Nm]	Leakage inductance [μH]
Combination 1	37.5	50.2	34.3
Combination 2	35.6	53.6	34.9
Combination 3	40.0	55.0	35.6
Combination 4	36.0	53.4	34.1
Combination 5	41.4	48.2	35.0

Combination 4 gave the best result for the rotor slot parameters. The combination provided high cranking torque and high boosting efficiency, at the same time as the leakage inductance and peak to peak torque ripple were kept low.

Operating Point 3 - Regeneration

The efficiency at operating 3 was also evaluated for the five combinations of rotor parameters presented in table 3.4. The simulation was done with sinusoidal voltage feeding and the result is presented in table 3.6.

Table 3.6: Efficiency at regeneration for the five combinations of rotor slot parameters.

Geometry	Efficiency [%]
Combination 1	87.9
Combination 2	88.0
Combination 3	87.6
Combination 4	88.0
Combination 5	88.1

All combinations gave efficiencies around 88 %. Combination 4 was then chosen for the final geometry for the 48 V IM since it gave the best result in terms of maximum torque, torque ripple and leakage inductance at the rerun of operating point 1, see table 3.5.

Stator and Rotor End Connections

Lastly, the leakage inductances and resistances of the end connections were calculated. The rotor short circuit ring resistance R_{scr} and rotor short circuit ring leakage inductance L_{scr} were calculated according to (2.9) and (2.11) as

$$R_{scr} = 0.84 \mu\Omega,$$

$$L_{scr} = 14 nH.$$

The stator end winding leakage inductance L_{ew} was calculated according to (2.3) as

$$L_{ew} = 11.7 \mu H.$$

The parameters used for the end connection calculations are presented in tables 3.7 and 3.2.

Table 3.7: Additional parameters used to calculate the end connection resistances and inductances.

Parameter	Description	Value
r_{scr}	Average radius of short circuit ring	45.00 mm
A_{scr}	Short circuit ring cross section area	4.00 mm ²
ρ_{al}	Aluminium resistivity	$2.86 \cdot 10^{-8} \Omega m$
l_{bar}	Rotor bar length	80.00 mm
l_s	Equivalent length of stator	80.00 mm
h_{ew}	Stator end winding height	15.00 mm
w_{ew}	Stator end winding width	108.00 mm
λ_{hew}	Height permeance factor	0.5
λ_{wew}	Width permeance factor	0.2

3.2.3 The 48 V PMSM Model

The 8-pole 48 V PMSM model originally created by [1] is presented in figure 3.6.

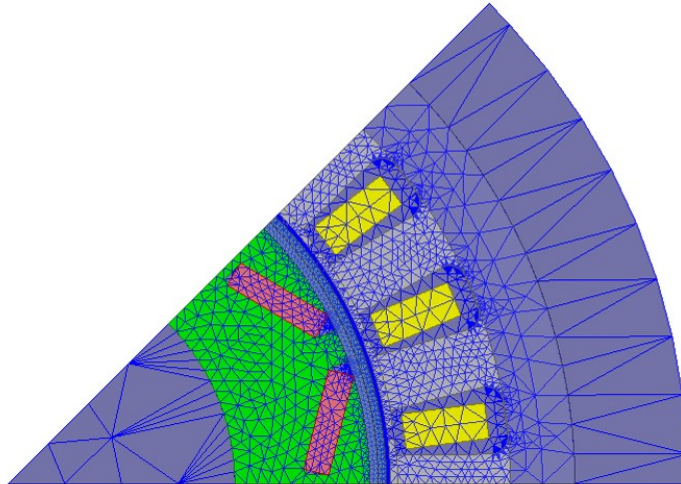


Figure 3.6: Geometry of the 48 V PMSM

The machine parameters that were changed from the original model are presented in table 3.8. The number of turns of the PMSM was changed from 3 to 14, in order to give the PMSM approximately the same nominal speed as the 48 V IM. The maximum stator current was set to 283 A, which was the same as for the 48 V IM.

Table 3.8: Parameters of the final geometry of the 48 V PMSM.

Parameter	Description	Value
w_{base}	Nominal speed	1520 rpm
n_s	Turns per slot	14
$I_{s,max}$	Maximum stator current	283 A
n_{max}	Maximum rotor speed	16 000 rpm

3.3 Parameter Identification from the Maxwell Models

To be able to develop a control algorithm that minimised the losses of the induction machine, the parameters of the circuit model in figure 2.4 were identified from the Maxwell model of the machine. The parameters of the circuit model were found through a no load simulation, a locked rotor simulation and a torque-slip simulation.

3.3.1 Identification of L_σ

The leakage inductance L_σ was determined through a locked rotor simulation in Maxwell. When the rotor was locked, $\omega_r = 0$, the magnetising reactance $\omega_s L_m$ and the core loss resistance R_c could be neglected since they were much larger than the rotor resistance R_r . The circuit model of the induction machine could then be simplified according to figure 3.7.

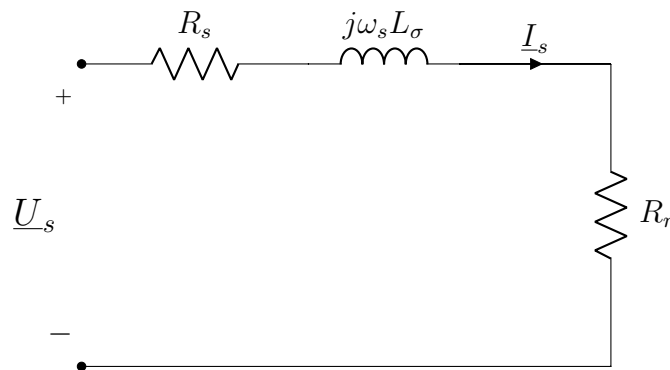


Figure 3.7: Locked rotor circuit model

To also determine if L_σ was dependent on the stator current I_s , the voltage amplitude was swept. The sweep was made between 10.6 and 31.8 V with a frequency of 50 Hz for the 400 V machine. The voltage of the 48 V IM was swept between 0.35 and 7.8 V with a feeding frequency of 66.67 Hz.

The leakage inductance was then determined from the total reactive power Q and the rms current in each phase as

$$L_\sigma = \frac{Q}{\omega_s (I_{sa}^2 + I_{sb}^2 + I_{sc}^2)}. \quad (3.1)$$

3.3.2 Identification of R_r

The rotor resistance R_r was determined from a simulation of the torque-slip curve at 50 Hz and 71 V for the 400 V machine and 66.67 Hz and 14.1 V for the 48 V machine. To detect the slip dependence the slip s was swept between -5 and 5 %.

For the calculation of R_r the full circuit model was used according to figure 2.4. The Maxwell simulation provided data of the stator current I_s , the stator voltage U_s and the torque T_{sim} . The rotor resistance R_r was determined from the magnetising voltage U_m with (2.22) rewritten as

$$T = \frac{n_p S}{\omega_s R_r} (|\underline{U}_{ma}|^2 + |\underline{U}_{mb}|^2 + |\underline{U}_{mc}|^2), \quad (3.2)$$

where

$$\underline{U}_m = \underline{U}_s - j\omega_s L_\sigma \underline{I}_s - R_s \underline{I}_s, \quad (3.3)$$

by minimising the error between T and the directly simulated torque from Maxwell T_{sim} with the least square method as

$$\min_{R_r} \sum_{i=1}^N (T(s_i) - T_{sim,i})^2, \quad (3.4)$$

where N is the number of simulation points.

3.3.3 Identification of L_m and R_c

The magnetising inductance L_m and the core loss resistance R_c were extracted from the Maxwell model through a no load simulation. During no load the electrical rotor speed ω_r equalled the angular supply frequency ω_s . The circuit model of the induction machine could then be simplified according to figure 3.8.

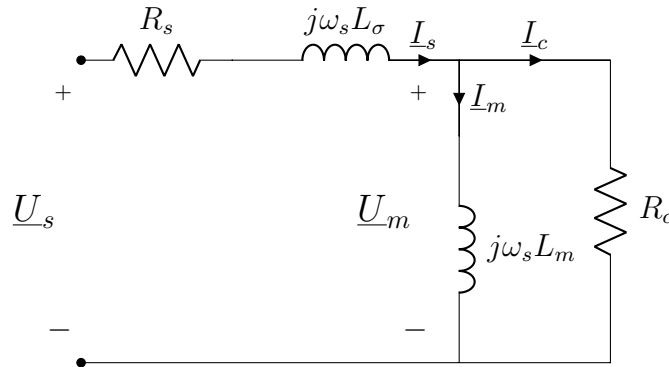


Figure 3.8: No load circuit model

The supply frequency f and the current amplitude I_s were swept during the simulation to determine the dependence of L_m and R_c on I_m and f . For the 400 V IM, f was swept from 5 to 80 Hz and I_s was swept from 1.4 to 32 A, resulting in 81 operating points. The corresponding sweep for the 48 V IM was done for 110 points, where f was swept from 8.33 to 533Hz and the voltage was adjusted such that the current was between 1 and 350 A.

Since $R_c \gg \omega_s L_m$ the magnetising current I_m was approximated to equal the stator current I_s during the no load test for calculation of both parameters. The magnetising inductance L_m was calculated from the reactive power Q as

$$L_m(f, I_m) = \frac{Q}{\omega_s(I_{sa}^2 + I_{sb}^2 + I_{sc}^2)} - L_\sigma, \quad (3.5)$$

where the leakage inductance L_σ was obtained from the locked rotor test in section 3.3.1. Since $I_m \approx I_s$, L_m was viewed to be in series with L_σ .

The core loss resistance R_c was calculated from the active core loss P_c as

$$R_c(f, I_m) = \frac{|\underline{U}_{ma}|^2 + |\underline{U}_{mb}|^2 + |\underline{U}_{mc}|^2}{P_c}, \quad (3.6)$$

where \underline{U}_m is given by (3.3).

3.3.4 Identification of $P_{r,stray}$

The parameter $P_{r,stray}(f, I_m)$ was introduced to account for stray losses in the rotor bars so that the induction machine circuit model would calculate the active losses more accurately. The rotor resistance R_r was identified from the torque-slip curve at 50 Hz to ensure that the circuit model would provide a torque that was as accurate as possible. However, the $R_r I_r^2$ -loss from the fundamental frequency used in the circuit model does not represent the entire active loss in the rotor bars due to stray losses, as discussed in section 2.4. To include these losses in the model the active loss in the rotor was modelled as

$$P_r = R_r I_r^2 + P_{r,stray}(f, I_m). \quad (3.7)$$

The stray loss $P_{r,stray}(f, I_m)$ was identified through the same no load simulation as L_m and R_c , which was presented in section 3.3.3. During the no-load test the fundamental frequency induces no currents in the rotor bars since $\omega_r = \omega_s$. The active losses in the rotor bars were thereby assumed to only be connected to the no-load stray losses

$$P_{r,noload} = P_{r,stray}(f, I_m). \quad (3.8)$$

3.4 Efficiency Map and Control Algorithm Set-up

The efficiency of the induction machine was evaluated over the entire torque-speed range during steady state. Each operating point (T_i, n_{ri}) within the range was connected to one efficiency η_i , as visualised in figure 3.9.

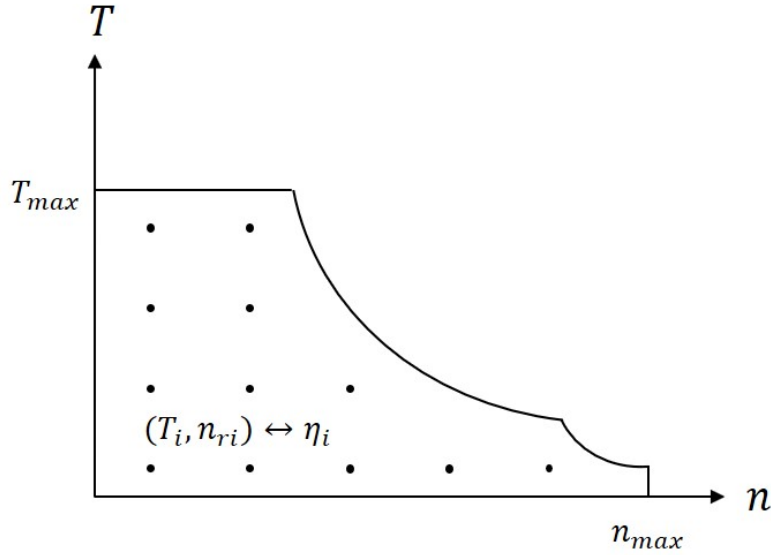


Figure 3.9: Torque-speed map of the induction machine

The efficiency was calculated by using a steady state reference control algorithm that minimised the losses in each operating point. The total losses of the induction machine P_{loss} can be expressed by summing (3.8) and (2.26),

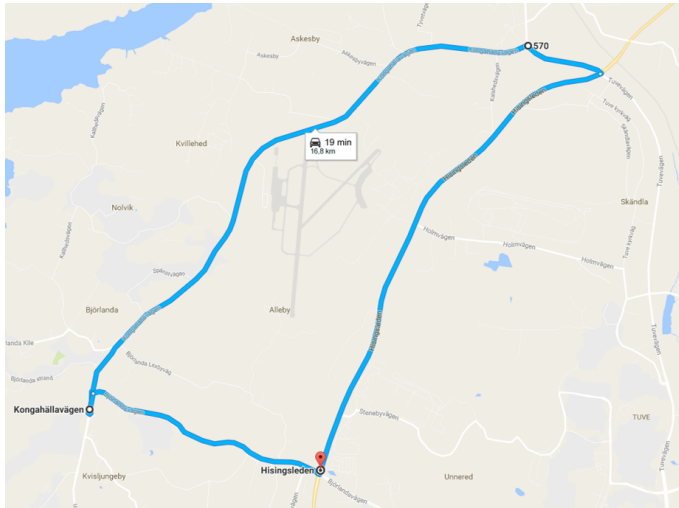
$$P_{loss} = R_d i_{sd}^2 + R_q i_{sq}^2 + P_{r,stray}. \quad (3.9)$$

The control algorithm that was used to create the efficiency maps utilised (3.9) together with (2.19)-(2.23) to find the stator voltage U_{si} and the supply frequency ω_{si} that minimised P_{loss} for the operating point (T_i, n_{ri}) . The algorithm was implemented with the Matlab function *fmincon* according to

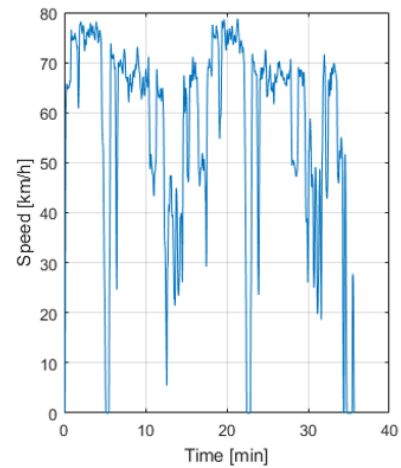
$$\min_{U_s, \omega_s} P_{loss}(T, n_r, U_s, \omega_s) : \begin{cases} u_{sd}^2 + u_{sq}^2 \leq U_{s,max}^2 \\ i_{sd}^2 + i_{sq}^2 \leq I_{s,max}^2 \\ T = T_i \\ n_r = n_{ri} \end{cases} \quad (3.10)$$

3.5 Drive Cycle Efficiency Set-up

The overall efficiency of the 48 V IM and the 48 V PMSM was evaluated for two different drive cycles in Gothenburg. The drive cycle data was taken from [4]. The first drive cycle was a highway route around Säve airport with light traffic and speed around 70 km/h. The cycle is presented in figure 3.10.



(a) Highway route



(b) Vehicle speed during highway driving

Figure 3.10: A highway drive cycle around Säve airport in Gothenburg.

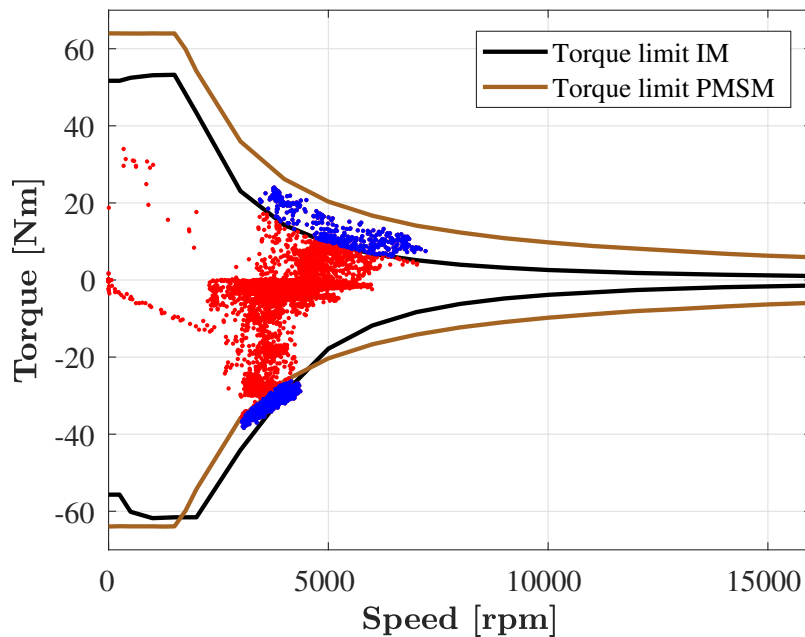


Figure 3.11: Torque-speed points for the Säve drive cycle. The red points lie within the maximum torque limit for both the PMSM and the IM. The blue points lie outside the maximum torque limit for either one or both machines.

3. Case Set-up

The operating points of the electric machine during the highway drive cycle are presented in figure 3.11 [4]. The operating points of the drive cycle data that were outside the torque range of either the 48 V PMSM or the 48 V IM are marked with blue colour in figure 3.11. The operating points from the drive cycle data that were within the torque range of both machines are marked with red colour.

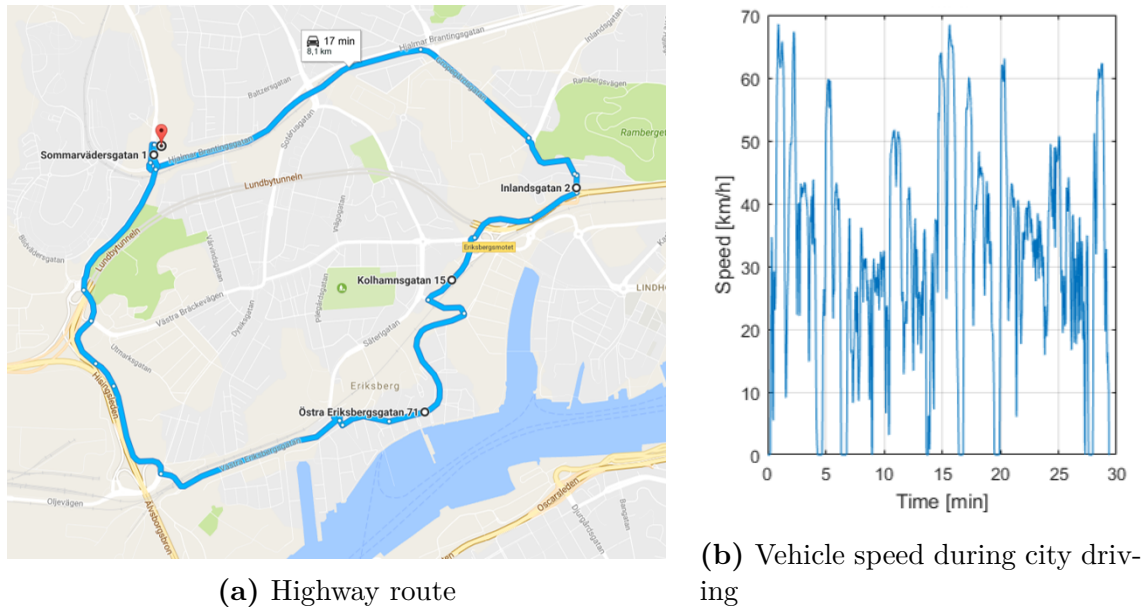


Figure 3.12: A city drive cycle around Lundby in Gothenburg.

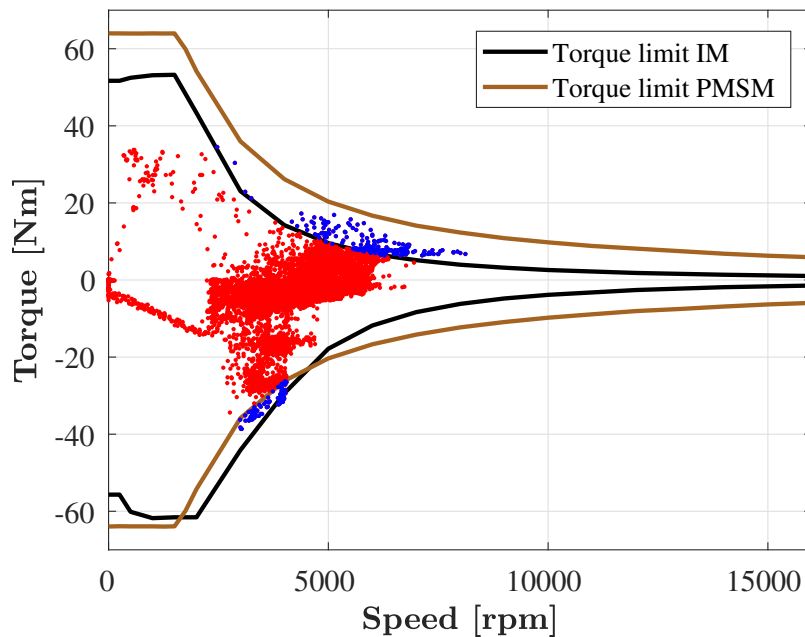


Figure 3.13: Torque-speed points for the Lundby drive cycle. The red points lie within the maximum torque limit for both the PMSM and the IM. The blue points lie outside the maximum torque limit for either one or both machines.

The second drive cycle was a city route around Lundby in Gothenburg, which is presented in figure 3.12. The route had medium traffic and speeds at 30-70 km/h. The operating points of the electric machines during the city drive cycle are presented in figure 3.13 in a similar way as for the highway drive cycle.

The drive cycle efficiency evaluation was done for two cases:

Case 1: The blue points were moved to the maximum torque that was available for both machines at that speed.

Case 2: The blue points were removed and only the red points were used.

During the driving cycles the electric machine was used both as a generator and a motor, as can be seen in figures 3.11 and 3.13. The total amount of energy at the shaft during motoring and generation is presented in table 3.9 for the two driving cycles. An additional mixed driving cycle containing 25 % city driving and 75 % highway driving was added for a cost comparison.

Table 3.9: Total amount of energy at the shaft during motoring and generation. The mixed driving cycle contains 25 % city driving and 75 % highway driving.

Drive Cycle	Recuperation energy $E_{mech,g}$		Boosting energy $E_{mech,m}$	
	Total [kWh]	Per km [Wh/km]	Total [kWh]	Per km [Wh/km]
Case 1: Highway	0.79	23.5	0.12	3.6
Case 1: City	0.61	37.6	0.12	7.4
Case 1: Mixed	0.75	27.0	0.12	4.6
Case 2: Highway	0.58	17.3	0.06	1.8
Case 2: City	0.59	36.4	0.097	6.0
Case 2: Mixed	0.58	22.1	0.07	2.9

The final drive cycle efficiency η_{DC} was then calculated as

$$\eta_{DC} = \frac{E_{mech,m} + E_{mech,g} - E_{loss,g}}{E_{mech,m} + E_{mech,g} + E_{loss,m}}, \quad (3.11)$$

where $E_{mech,m}$ and $E_{mech,g}$ were the total mechanical output energy during motoring and generation found in table 3.9, $E_{loss,m}$ was the total losses during motoring and $E_{loss,g}$ was the total losses during generation. The loss values were obtained by interpolating the torque-speed points in the drive cycle to the loss maps of the electric machines.

3.6 Sustainability Set-up

The sustainability analysis was done from three perspectives:

1. A social perspective
2. An economical perspective
3. An ecological perspective

Further on, the sustainability comparison of the two machines was based on the efficiencies of the machines and the active materials inside the machines. The investigated materials were copper (used in stator winding), aluminium (used in the rotor bars of the IM), NdFeB-magnets (used in the rotor of the PMSM) and electrical steel (used for the magnetic path in the rotor and the stator). However, the steel was only included in the cost analysis. The comparison of the active materials was limited to the steps before the materials entered the motor factory as visualised in figure 3.14, a cradle to gate analysis.

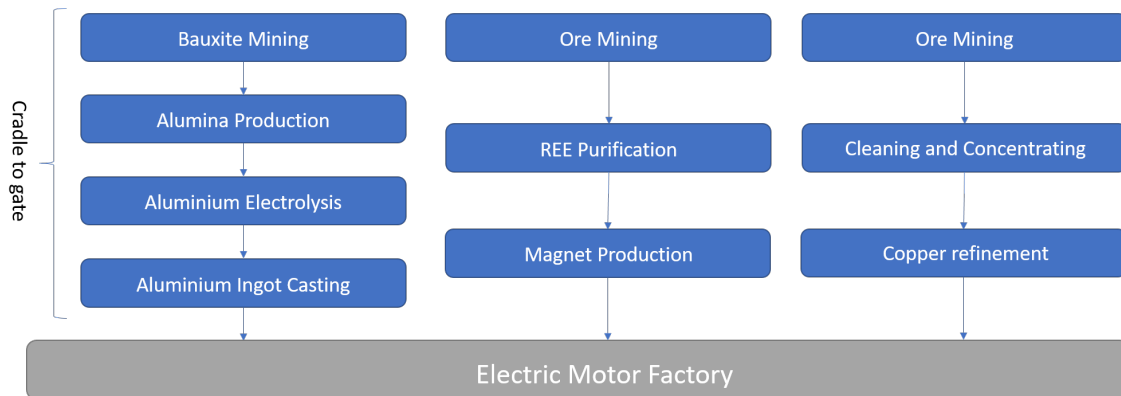


Figure 3.14: Production steps for primary aluminium, copper and NdFeB-magnets. The blue boxes are included in the sustainability comparison and represents the steps from mining of the ore until being bought by a factory (cradle to gate).

4

Verification of the Maxwell Model of the 400 V IM

From [23] there were several measurements available for the 400 V machine. In order to verify that the Maxwell model of the 400 V IM was properly representing the actual machine, the T-model circuit parameters from the simulations in Maxwell were compared to the parameters extracted from the available measurements. Analytical calculations based on the machine geometry were also included in the verification. The T-model parameters of the 400 V IM are compared in table 4.1.

Table 4.1: T-model circuit parameters from measurements, simulation and analytical calculations for the 400 V IM.

Parameter	Description	Measured	Simulated	Analytical	Unit
R_s	Stator resistance	0.184	0.184	0.184	Ω
R_{rT}	Rotor resistance	0.174	0.155	0.158	Ω
L_{mT}	Magnetising inductance	41.3	47.6	50.7	mH
$L_{s\lambda}$	Stator leakage inductance	2.55	1.82	1.03	mH
$L_{r\lambda}$	Rotor leakage inductance	2.00	1.82	0.86	mH
R_c	Core loss resistance	130	276	-	Ω
f_s	Frequency	43.5	43.5	-	Hz
U_{LL}	L-L rms voltage	288	288	-	V

The simulated circuit parameters matched the measured parameters rather well. The analytical values were overall close to the simulated values if the leakage inductance was excluded. The rotor resistance was 11 % lower in the simulation than in the measurements, while the magnetising inductance was 15 % higher in the simulation. This means that the real machine will produce a lower torque than what is predicted in the simulation if the voltage and frequency are the same.

The leakage inductance in both the rotor and the stator was significantly smaller for the simulated values compared with the measured values. One reason to this was the disregarding of the end winding inductance in the stator. Another was that the machine in the simulation had no skewing which also contributes to a lower leakage inductance [15]. The analytic values were even lower, only approximately 50 % of the measured values. The majority of the difference was believed to be due to the

disregarding of the differential leakage. According to [15] this typically accounts for 30-50 % of the total stator leakage and 25-45 % of the total rotor leakage inductance in a 6 pole induction machine with a power rating of 10-50 kW.

The core loss resistance was higher for the simulation than the measurements. This led to lower core losses in the simulation model than in the actual machine. It was believed that the increase in core loss for the real IM was caused by manufacturing defects when cutting and welding the laminations. According to [24] both welding and cutting could increase the iron loss as much as 50 %.

4.1 Measurements

The measurements of parameter values for the comparison were taken from [23]. Some parameters had been given temperature, current and frequency dependencies. However, only a single value for each parameter was used from the measurements to compare with the simulated and analytically calculated values. The measured values were chosen according to the following conditions:

- R_s was measured at 20 °C.
- R_{rT} was extracted from a load test at 43.5 Hz and 288 V L-L rms voltage where the slip was varied from rated torque in motor mode to rated torque in regeneration mode.
- $L_{s\lambda}$ was taken as the value given by the manufacturer.
- $L_{r\lambda}$ was extracted from a locked rotor test at 20 A and 10 Hz, taking the total leakage inductance and subtracting $L_{s\lambda}$.
- L_{mT} was extracted from a no-load test at 43.5 Hz, 288 V L-L rms and 40 °C.
- R_c was extracted from a no-load test at 43.5 Hz, 288 V L-L rms.

4.2 Simulations

The circuit parameters from the simulation were extracted using the same methodology and tests as in the measurements with a few exceptions. R_s was calculated analytically using (2.1) with the parameters from table 3.1 and 4.2. Instead of assuming a value of $L_{s\lambda}$, the total leakage inductance from the locked rotor test was assumed to be equally distributed between the rotor and the stator.

4.3 Analytical Calculations

The analytical values for the T-model circuit parameters were calculated using the method described in section 2.1 and the parameters presented in table 3.1. Addi-

tional parameter used are presented in table 4.2.

Table 4.2: Additional parameters for the 400 V IM used for the analytic calculations

Parameter	Description	Value
r_{scr}	Average radius of short circuit ring	86.70 mm
A_{scr}	Short circuit ring cross section area	325.00 mm ²
ρ_{al}	Aluminium resistivity	$2.86 \cdot 10^{-8} \Omega\text{m}$
ρ_{cu}	Copper resistivity	$1.68 \cdot 10^{-8} \Omega\text{m}$
l_{bar}	Rotor bar length	230.00 mm
l_s	Equivalent length of stator	230.00 mm
h_{ew}	Stator end winding height	40.00 mm
w_{ew}	Stator end winding width	100.00 mm
λ_{hew}	Height permeance factor	0.5
λ_{wew}	Width permeance factor	0.2
$A_{r,slot}$	Rotor slot area	76.42 mm ²
A_{cu}	Conductor copper area	1.96 mm ²
l_{ew}	Conductor copper area	19.96 mm
γ_p	Pitch angle	0 rad
h'_{gap}	Effective air gap length	6.16 mm

5

Result

In this chapter the result of the thesis work is presented. This includes circuit model parameters for the 48 V and 400 V IMs, evaluation of the steady state control algorithm and a comparison between the 48 V IM and the 48 V PMSM. The comparison was made based on efficiency, torque performance, power performance and sustainability.

5.1 Identified Induction Machine Circuit Parameters

Using the method described in section 3.3 circuit model parameters corresponding to the model presented in figure 2.5 were determined.

5.1.1 The 400 V IM

The identified circuit model parameters of the 400 V induction machine are presented in table 5.1.

Table 5.1: Simulated IM circuit model parameters for the 400 V IM.

Parameter	Description	Simulated Value
R_s	Stator resistance	0.184 Ω
R_r	Rotor resistance	0.145 Ω
L_σ	Leakage inductance	3.68 mH
$L_m(I_m)$	Magnetising inductance	20.6-46.0 mH
$R_c(f, I_m)$	Core loss resistance	37.5-332 Ω
$P_{r,stray}(f, I_m)$	Rotor stray loss compensation	0-690 W

5. Result

The leakage inductance L_σ was calculated according to (3.1) and the result is presented in figure 5.1.

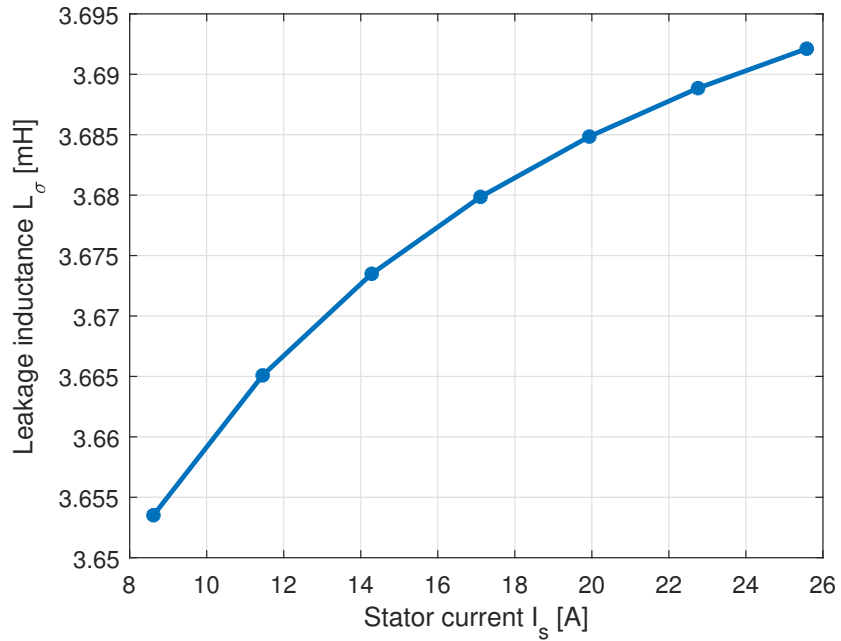


Figure 5.1: Current dependence of the leakage inductance for the 400 V IM.

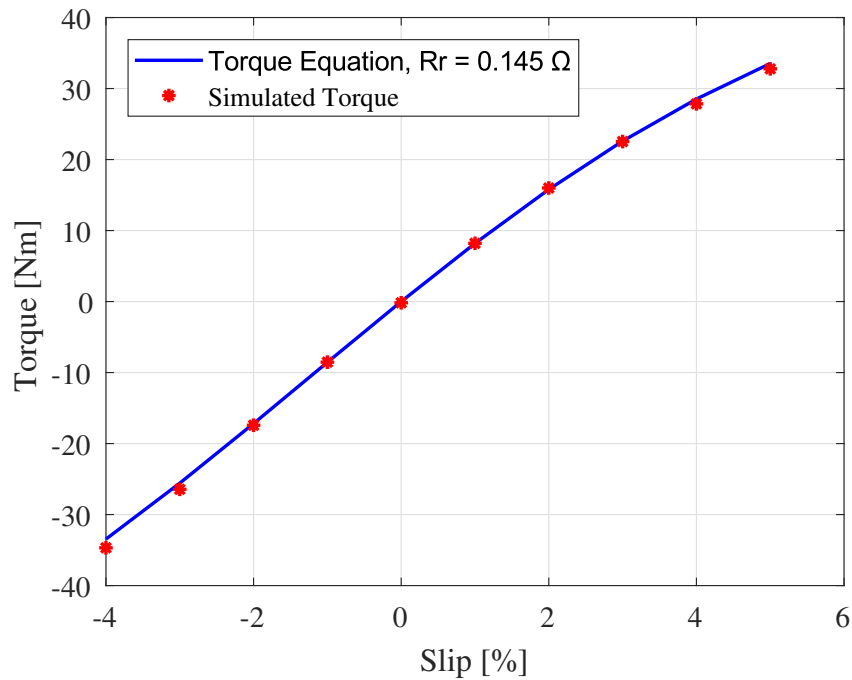


Figure 5.2: Slip dependence of the torque with 71 V applied phase voltage for the 400 V IM.

The leakage inductance had nearly no dependence on the stator current during the locked rotor test. The value deviated no more than 0.04 mH within the operating range. The inductance value was therefore chosen as the mean value,

$$L_{\sigma} = 3.68 \text{ mH}.$$

The rotor resistance R_r was calculated by fitting (3.2) to the simulated torque values T_{sim} according to the least square method. The fit between the torque equation and the simulation data is shown in figure 5.2. The best fit was found with the rotor resistance

$$R_r = 0.145 \Omega.$$

The magnetising inductance $L_m(f, I_m)$ was calculated according to (3.5) and the result is presented in figure 5.3. There was hardly any frequency dependence and therefore L_m was chosen as the interpolated function of I_m at 50 Hz,

$$L_m(f, I_m) \equiv L_m(f = 50\text{Hz}, I_m) = L_m(I_m). \quad (5.1)$$

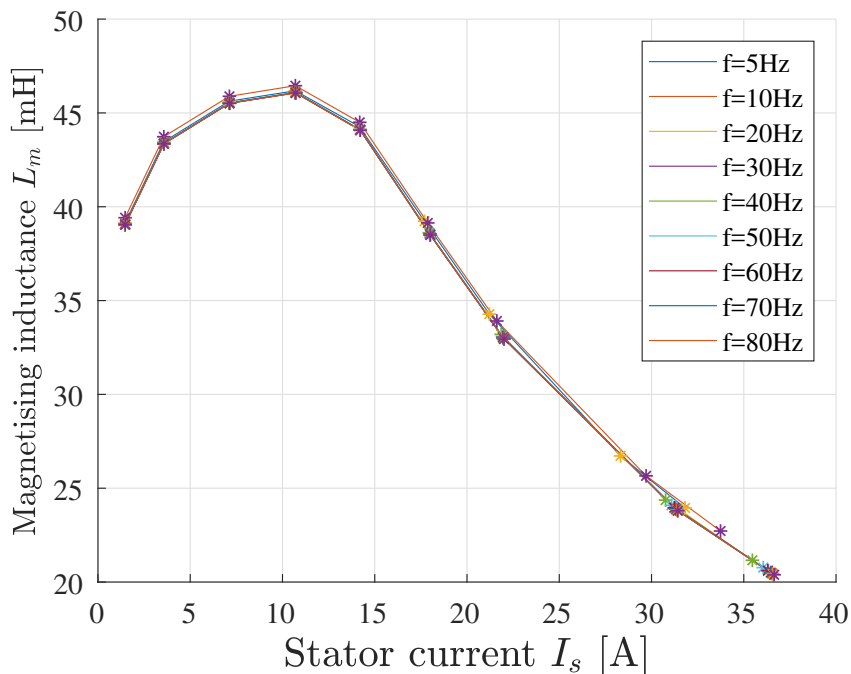


Figure 5.3: Current dependence of the magnetising inductance L_m for the 400 V IM. The asterisks are the simulation data points.

The core loss resistance $R_c(f, I_m)$ was calculated from (3.6) and the result is presented in a 3D-plot in figure 5.4. The resistance was dependent on both the magnetising current I_m and the supply frequency f . Thereby R_c was chosen as an interpolated 3D-surface from the simulation data.

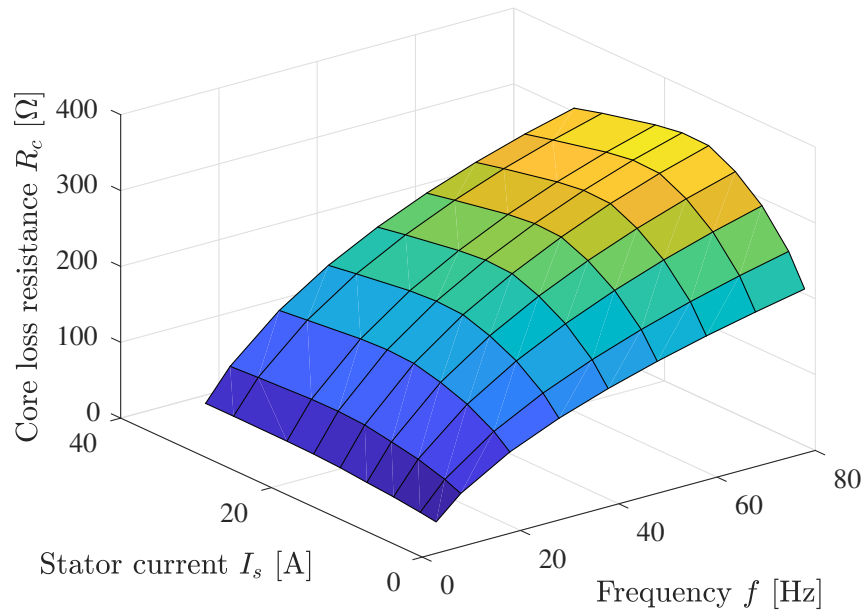


Figure 5.4: Current and frequency dependence of the core loss resistance R_c for the 400 V IM.

The no-load stray loss in the rotor bars $P_{r, stray}(f, I_m)$ is presented in figure 5.5 and was identified through the same no-load simulation as R_c and L_m , which was presented in section 3.3.3. The loss depended strongly on both the magnetising current I_m and the supply frequency f . It reached 690 W at 80 Hz and 32 A.

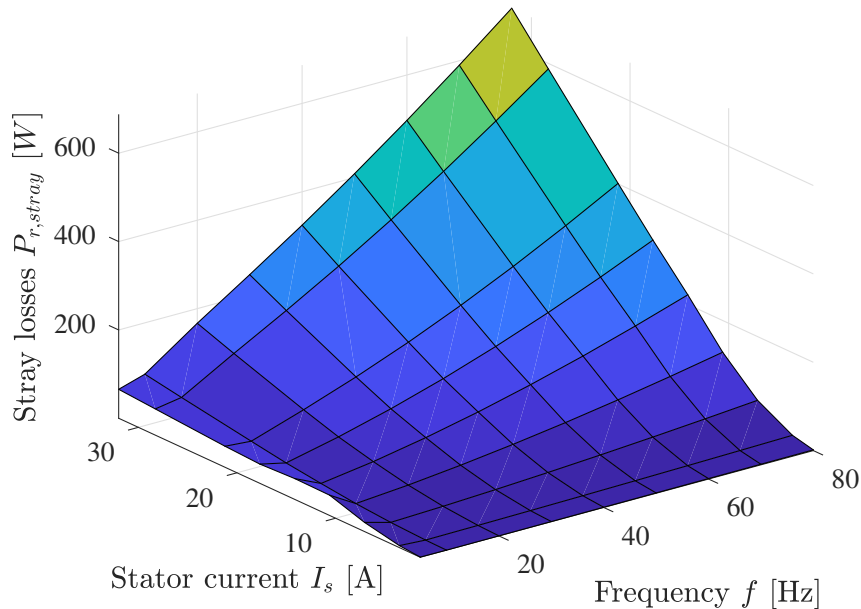


Figure 5.5: Current and frequency dependence of the no-load stray loss in the rotor bars $P_{r, stray}$ for the 400 V IM.

5.1.2 The 48 V IM

A list of all circuit model parameters for the 48 V IM are presented in table 5.2.

Table 5.2: Simulated circuit model parameters for the 48 V IM.

Parameter	Description	Simulated Value
R_s	Stator resistance	6.7 m Ω
R_r	Rotor resistance	3.5 m Ω
L_σ	Leakage inductance	61 μ H
$L_m(I_m)$	Magnetising inductance	0.12-0.61 mH
$R_c(f, I_m)$	Core loss resistance	1-9 Ω
$P_{r, stray}(f, I_m)$	Rotor stray loss compensation	0-550 W

The leakage inductance L_σ was calculated according to (3.1) and the result is presented in figure 5.6.

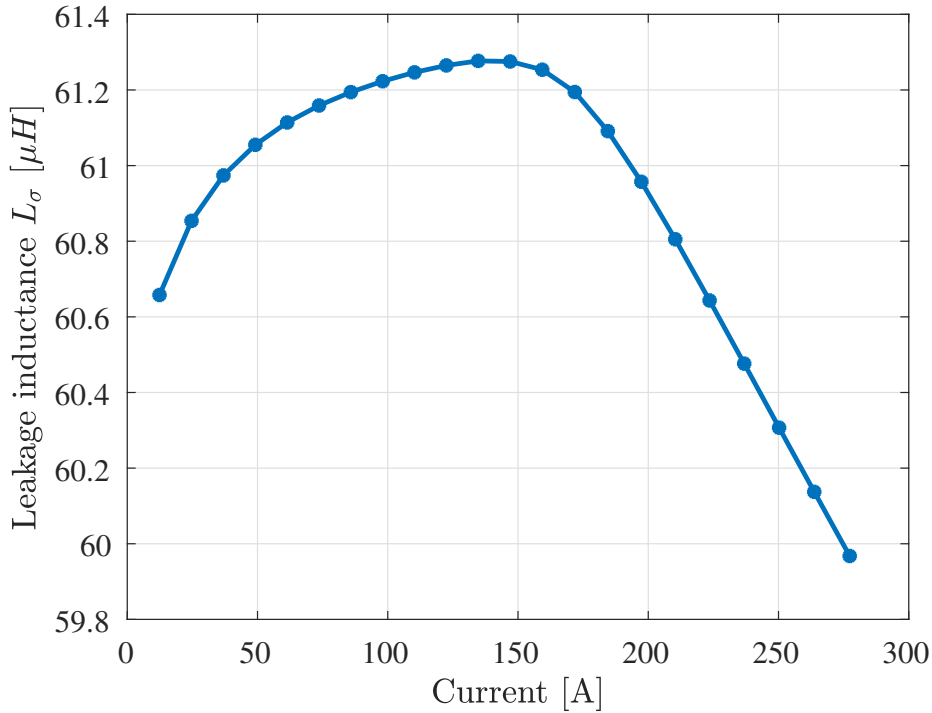


Figure 5.6: Current dependence of the leakage inductance for the 48 V IM.

The leakage inductance had a small current dependency and deviated around 2% from its mean value. However, for simplicity the leakage inductance was chosen as the mean value,

$$L_\sigma = 61 \mu H.$$

The rotor resistance R_r was determined using (3.4). Figure 5.7 shows the simulated torque together with a curve fit of (3.2) to the simulation points using

$$R_r = 3.5 m\Omega,$$

which was the best fit. All simulated torque points had a lower value than the fitted curve, between 0.8 and 2.2 Nm lower. According to [25] the slots in the machine cause harmonic fields that produce a negative torque, even at no-load. However, in (3.2) that was used for torque estimation in the circuit model, the torque was always zero at zero slip. This led to a difference between the simulated and estimated torque, which can be seen in figure 5.7. It is also shown by [25] that the negative torque is current dependent, which could explain the bigger disparity for larger slips where the current was higher. The negative torque was also present in the case of the 400 V machine, as can be seen in figure 5.2. The effect was much smaller for the 400 V machine, possibly due to lower current and smaller slot openings.

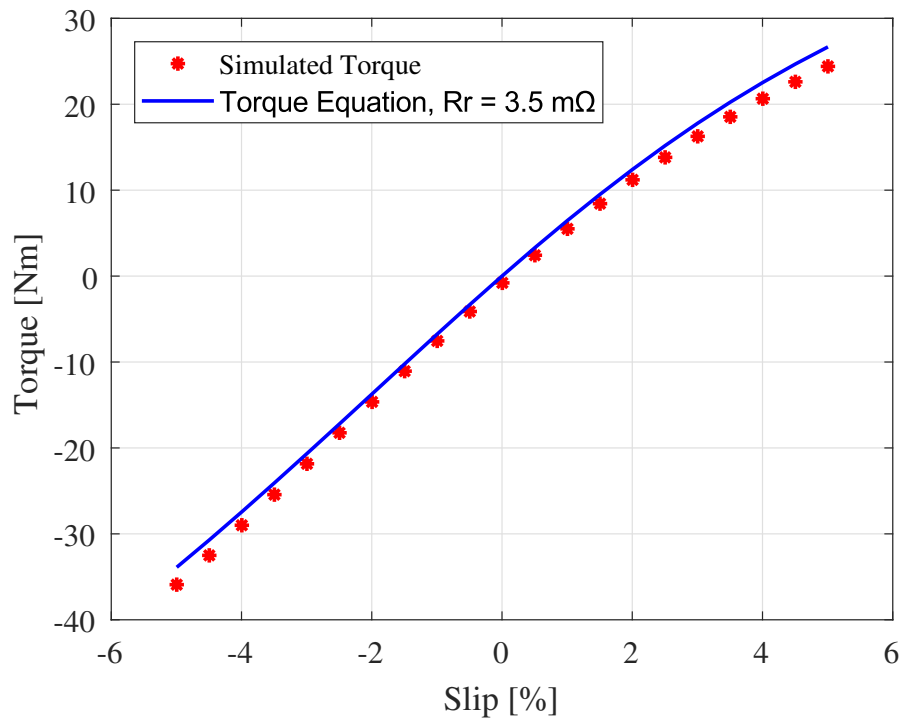


Figure 5.7: Slip dependence of the torque with 14 V applied phase voltage for the 48 V IM.

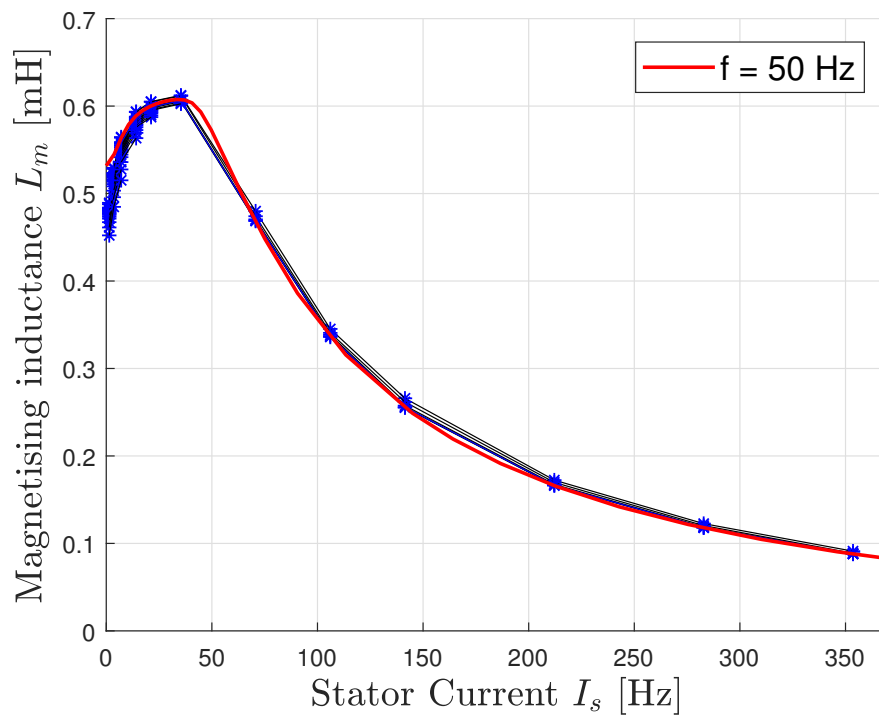


Figure 5.8: Current dependence of the magnetising inductance L_m for the 48 V IM.

The magnetising inductance L_m was calculated according to (3.5) and the result is presented in figure 5.8. The blue stars represent L_m at all simulation points and the red curve represents L_m at 50 Hz. Note that the red curve was extracted from a separate no load simulation at 50 Hz with additional current points.

For speeds below 4000 rpm there was hardly any frequency dependence for L_m , however for higher frequencies L_m decreased with increased frequency. The difference was at most 0.05 mH at low currents (which was where the high speed points were located because of the voltage limit). It was unknown why this occurred, but one possible explanation could be that the approximation $I_m \approx I_s$ used for the extraction of L_m leads to a significant error at higher speeds. A considerable part of the current could have been directed along the q-axis for high speeds. However, the frequency dependence difference was neglected and L_m was taken at 50 Hz as shown in figure 5.8.

The core loss resistance R_c was determined according to (3.6) for each simulation point. Since R_c was both current and frequency dependant the value was taken as the interpolated surface of these points and is presented in figure 5.9. Similar to R_c , the rotor bar no-load stray loss component $P_{r,stray}$ was chosen as the interpolated surface of the individual points and is shown in figure 5.10.

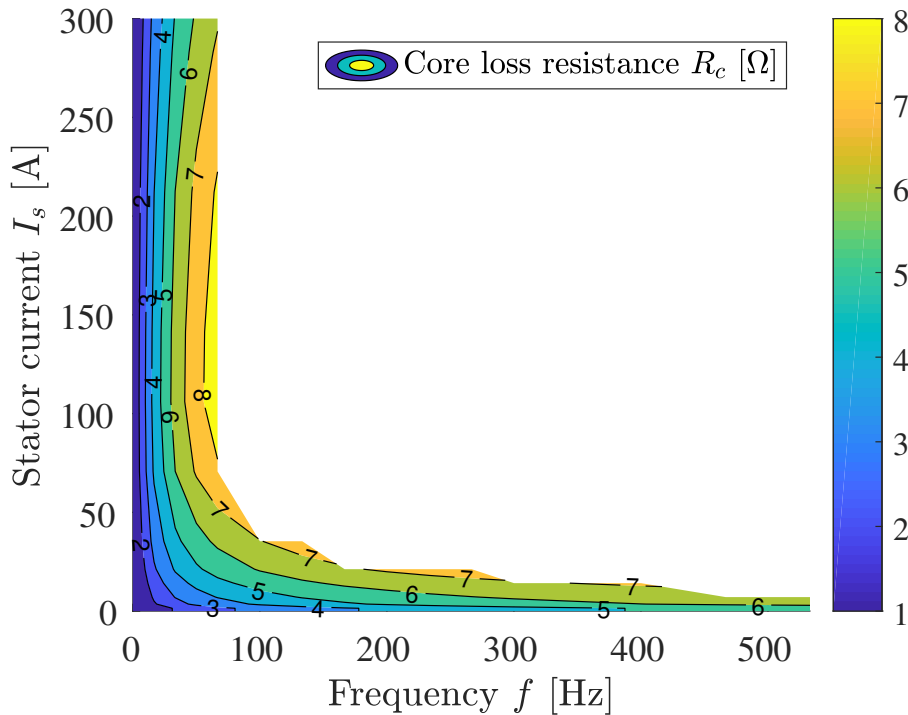


Figure 5.9: Current and frequency dependence of the core loss resistance R_c for the 48 V IM. The resistance varied between 1-8 Ω .

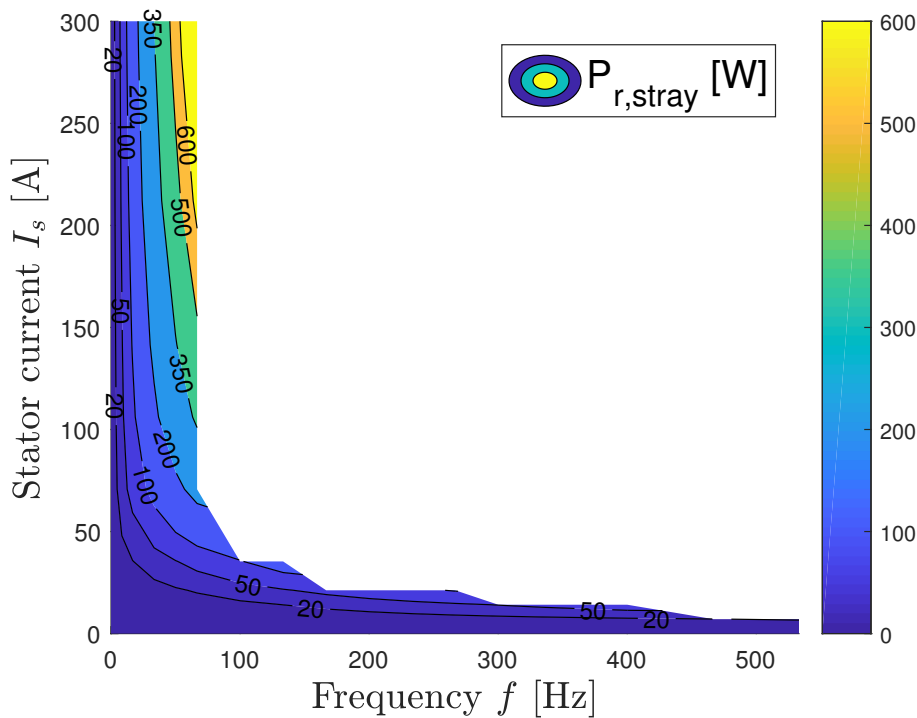


Figure 5.10: Current and frequency dependence of the no-load stray loss in the rotor bars $P_{r, \text{stray}}$ for the 48 V IM. The loss varied between 0-600 W.

5.2 Efficiency Evaluation and Comparison to Circuit Model

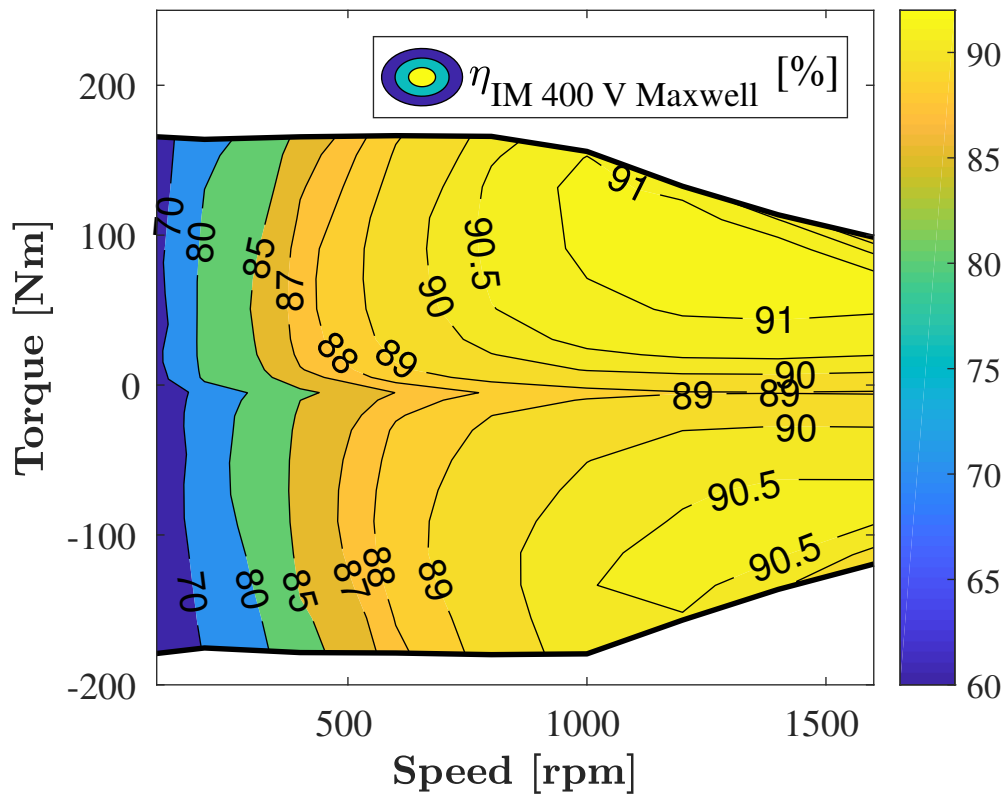
By using the steady state control algorithm presented in section 3.4 estimations for U_s and ω_s were found for each torque-speed point. The speed was swept from 100 rpm to 1600 rpm for the 400 V induction motor and from 250 to 16000 rpm for the 48 V IM. At every speed point the torque was swept from the minimum to the maximum torque calculated by the algorithm.

5.2.1 The 400 V IM

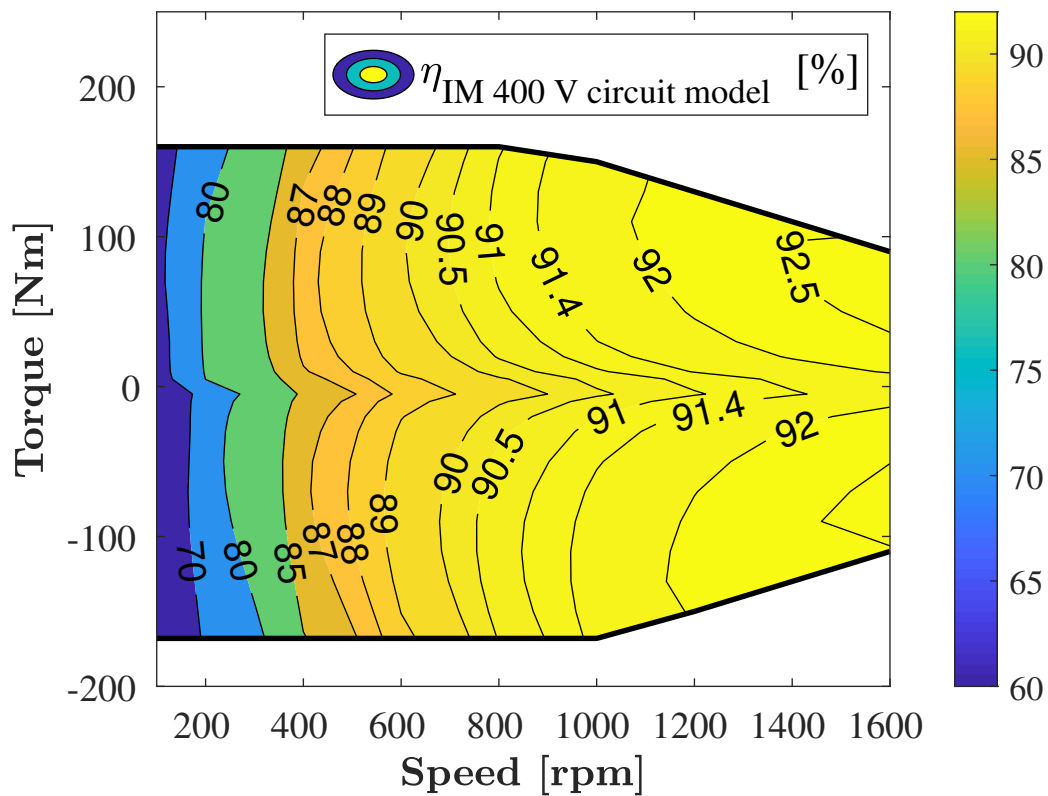
The efficiency map from the actual torque and losses in Maxwell can be seen in figure 5.11a. Figure 5.11b shows the efficiency map for the same torque speed points calculated by the steady state algorithm using the circuit model. The difference in efficiency was greatest for high torque and high speeds where it differed with around two percentage points. For lower torques and speeds the difference was much smaller. At 600 rpm and 30 Nm the circuit model efficiency was 89.59 % and the efficiency from Maxwell was 89.38 %. It was believed that the relatively bad match at high speeds and torques came from additional stray losses that were not included in the circuit model.

Another thing to note was that the efficiency at zero torque should be 0 %. However, because figure 5.11 was interpolated and the lowest amplitude of the torque was 5 Nm, this was not the case in the presented efficiency maps. Since no mechanical losses were considered, the efficiency was still only a few percentage points lower compared to the efficiency maps at very low torques (~ 0.1 Nm).

There was also a difference in the maximum torque between motoring and generation mode. In motoring mode the maximum torque was 162 Nm while the maximum torque in generation mode was 178 Nm. When the machine was in generation mode the current flowed out of the machine causing a negative voltage drop over R_s and L_σ in figure 2.4, allowing the back-EMF to be higher than the terminal voltage. On the contrary, in motoring mode the current flowed in to the motor causing a voltage drop over R_s and L_σ , and thereby reducing the maximum back-EMF.



(a) Maxwell efficiency map



(b) Circuit model efficiency map

Figure 5.11: Efficiency maps for the 400 V IM

5. Result

The losses were divided into three parts; stator winding losses, rotor bar losses and core losses, as described in section 2.3. Loss maps for these losses including the total losses are presented in figure 5.12 and 5.13. Figure 5.12 shows the losses from Maxwell, while figure 5.13 shows the predicted model losses. The model predicted the copper losses very well over the whole region. The rotor bar losses and the core losses were not as well predicted at high speeds, which was also why the efficiency was not as well predicted in that area. At low speeds the stator winding and rotor bar losses dominated the total losses. When the speed increased the heavily frequency dependent core losses started to affect the total losses considerably.

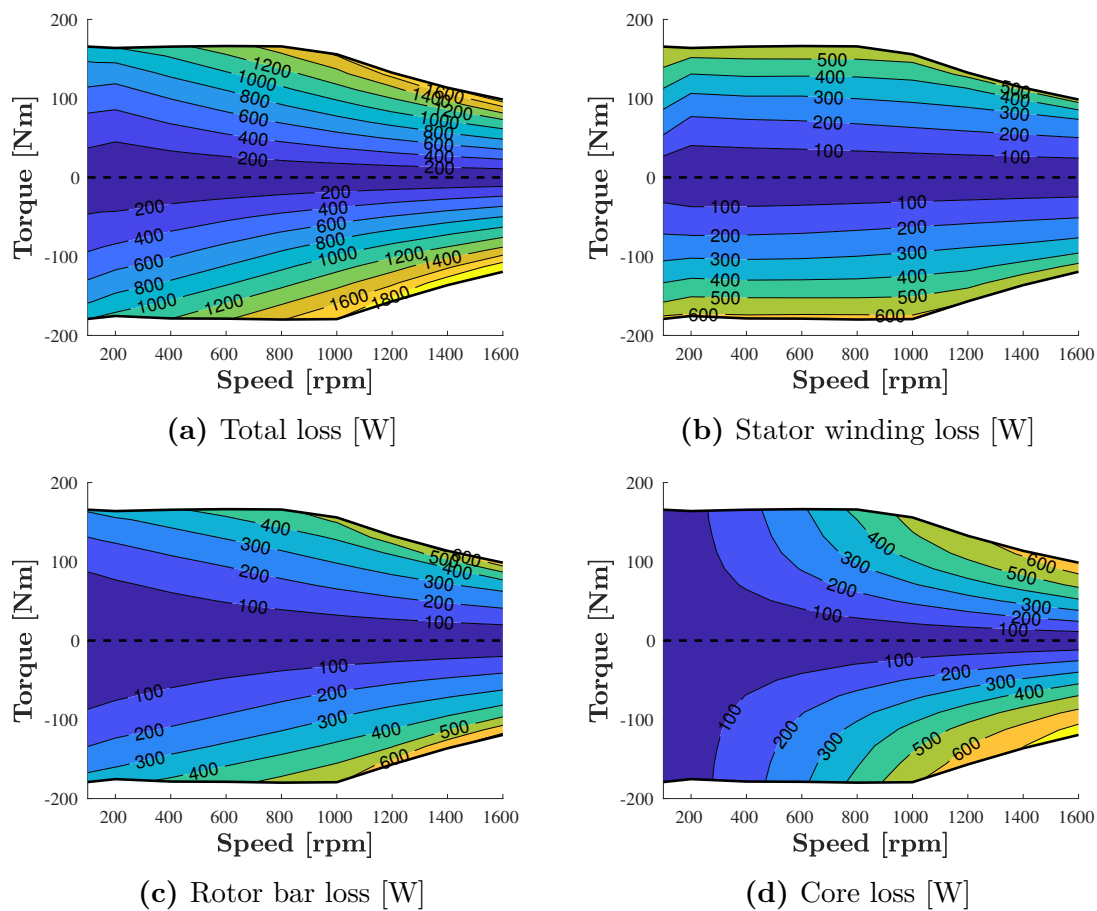


Figure 5.12: Losses in different parts of the 400 V IM from Maxwell

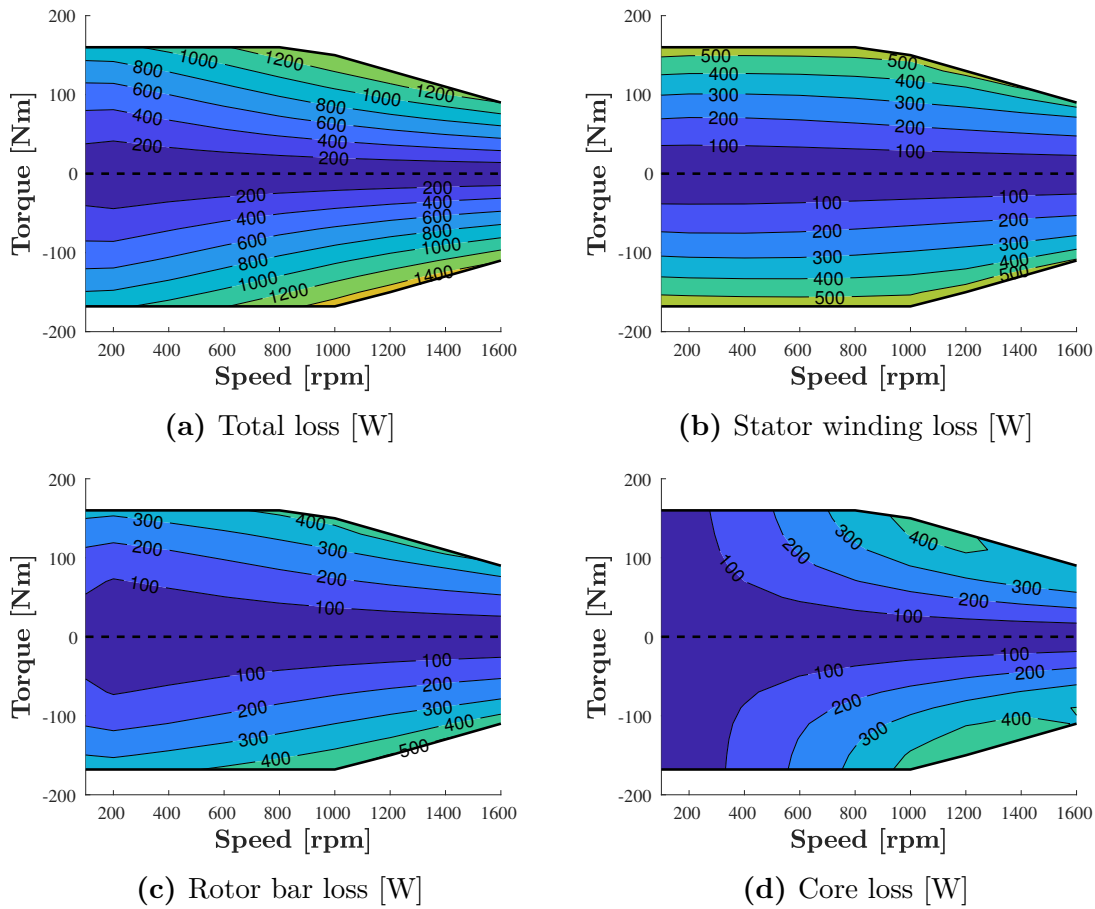


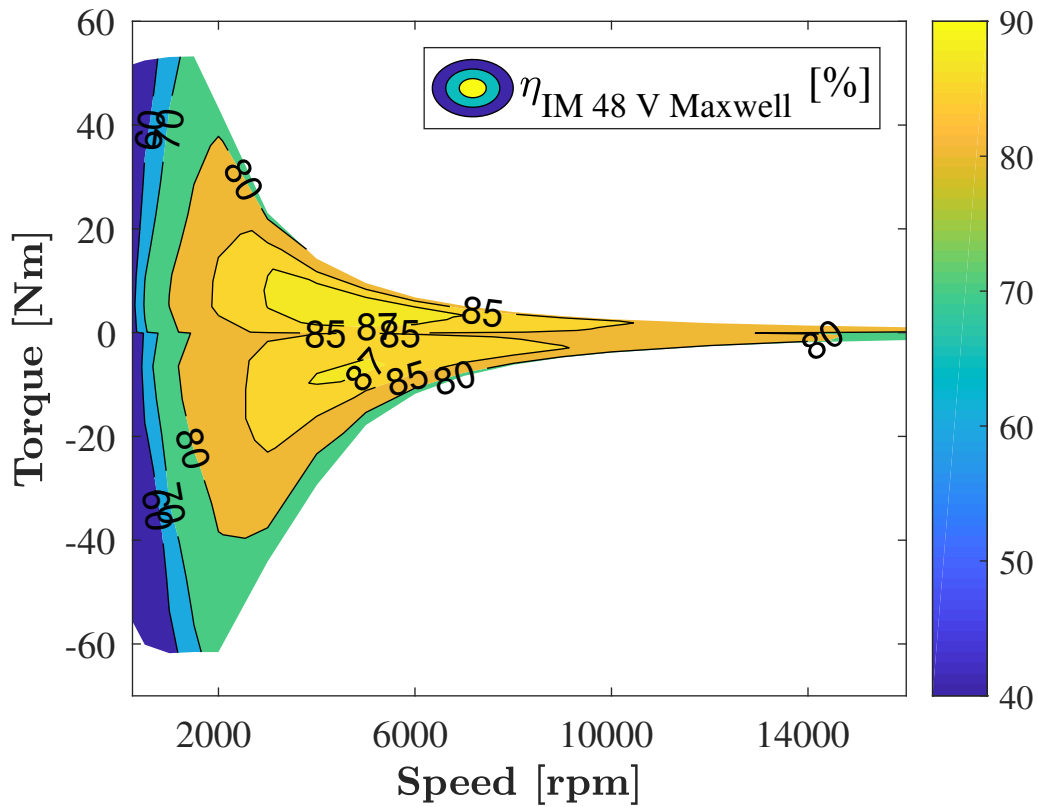
Figure 5.13: Losses in different parts of the 400 V IM from circuit model

5.2.2 The 48 V IM

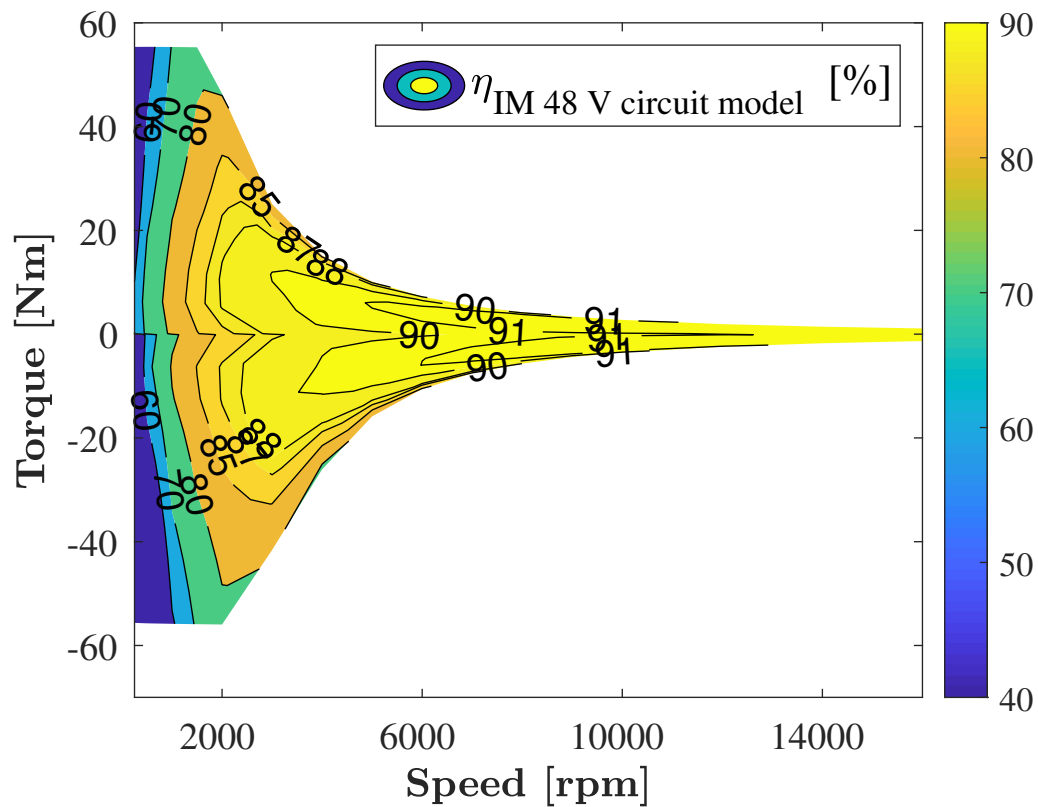
The efficiency of the 48 V IM, extracted from the simulation result in Maxwell, is presented in figure 5.14a. The corresponding estimated efficiency from the circuit model is presented in figure 5.14b. Figure 5.15 visualise the difference between the simulated and estimated efficiency.

Similar to the 400 V IM the difference in efficiency was the largest at high speeds. At 15000 rpm the difference was over 10 percentage points, which was believed to be caused by stray losses not included in the circuit model. For low speeds there was still a significant error in efficiency which was not present in the 400 V machine. This was believed to be due to an under estimation in current, which lead to an underestimation in stator winding loss and rotor bar loss. This can be observed comparing figures 5.16 and 5.17. The difference between the model-efficiency and the Maxwell-efficiency was generally smaller during generation. This indicates that the underestimation in torque shown in figure 5.7 was responsible for some of the efficiency disparities.

From the simulation in Maxwell the maximum torque was 56 Nm in motoring mode and 62 Nm in generation mode which can be seen in figure 5.14a. The maximum torque was not constant up until the field weakening point as expected, instead the torque was increasing. The reason for this was that the current was not constant at the current limit of 283 A as the algorithm was trying to set it to. During motoring mode the current went from an overcurrent of 3 % at 250 rpm to a 5 % overcurrent at 1500 rpm. In generation mode the current went from an undercurrent of 3 % at 250 rpm to an overcurrent of 8 % at 1500 and 2000 rpm. At lower torques the current was closer to the predicted value and was generally slightly lower than what was expected from the algorithm.



(a) Maxwell efficiency map



(b) Circuit model efficiency map

Figure 5.14: Efficiency maps for the 48 V IM

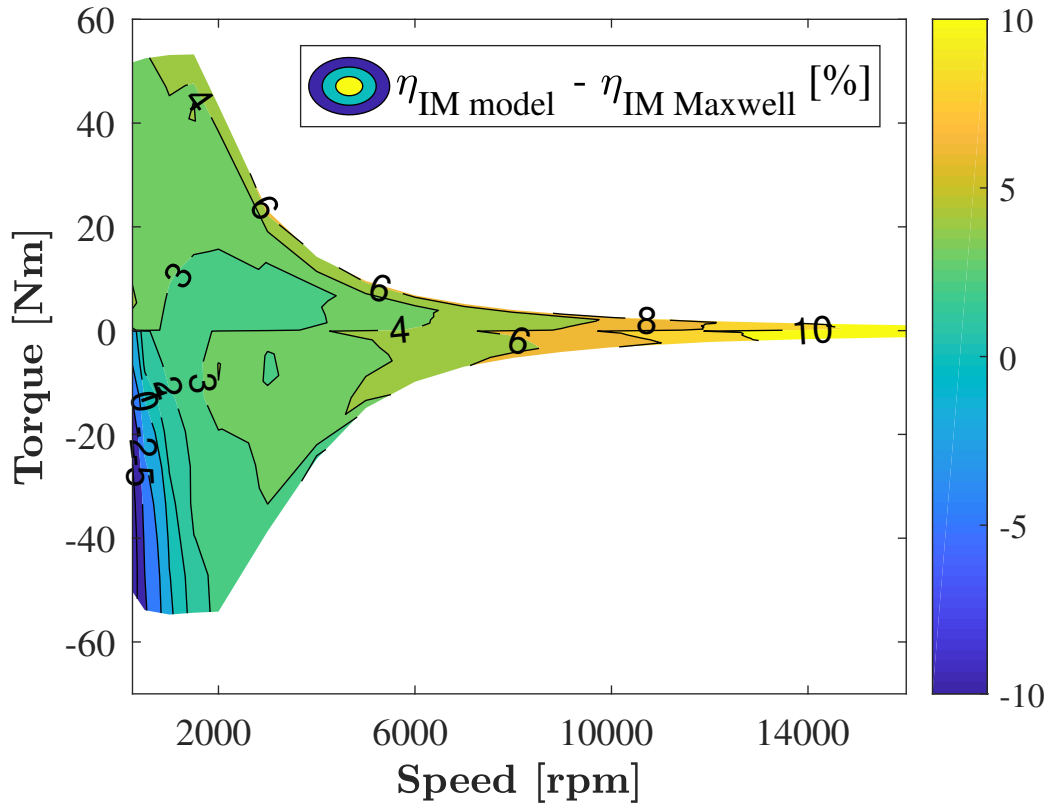


Figure 5.15: Error in efficiency between Maxwell simulation and circuit model in percentage points for the 48 V machine

The circuit model's ability to predict the losses was useful but was more or less irrelevant for the comparison with the PMSM. Instead, it was important that the efficiency map from Maxwell in figure 5.14a contained the most efficient points and that the maximum torque was found for each speed point. A few points were selected and tested in order to find how close the efficiency was to the maximum possible efficiency. The efficiency difference is presented in table 5.3.

Table 5.3: Simulated efficiency of the 48 V IM using voltage and slip determined by the minimum loss algorithm compared to the optimal voltage and slip.

Torque [Nm]	Speed [rpm]	Efficiency	Maximum efficiency
27.5	1000	74.8	74.8
-5	2000	86.1	86.3
5	4000	87.4	87.6
-20	4000	84.5	84.5
1	10000	85.1	85.6
-1	10000	86.2	86.7

The efficiency deviation from the optimal efficiency in Maxwell increased with speed and had a maximum deviation of 0.5 percentage points for the investigated torque-

speed points. Generally, lowering the slip and increasing the voltage gave a better efficiency, compared to what the algorithm predicted. This implied that the q-current should be lowered while increasing the d-current in order to reach the maximum efficiency. One reason for why the algorithm predicted a too high q-current was believed to originate from the disregarding of load stray losses, which were likely to have a q-current dependence. This led to that the algorithm were not penalising the q-current enough, especially at high speeds.

The losses of the 48 V IM in the different parts of the motor are presented in figure 5.16 for the Maxwell simulation and figure 5.17 for the circuit model. At lower speeds the total loss was dominated by the winding loss and the rotor bar loss. At high speeds the core loss was of great importance and was around half of the total losses.

As previously mentioned, the algorithm predicted the high speed efficiency badly. By comparing figure 5.16 and 5.17 it is clear that the efficiency error originated from large errors in core losses and rotor bar losses. The losses at the maximum frequency were over three times higher for both the rotor bar loss and the core loss.

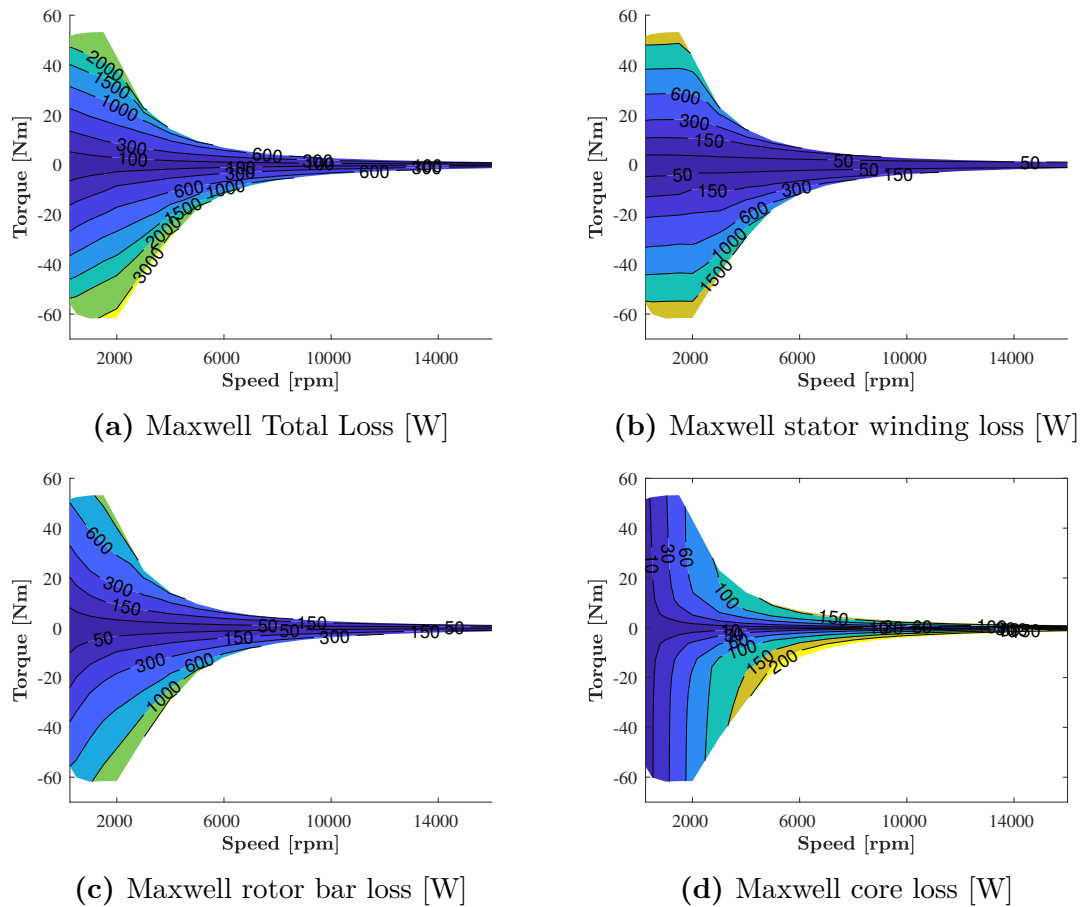


Figure 5.16: Losses in different parts of the 48 V IM from Maxwell

5. Result

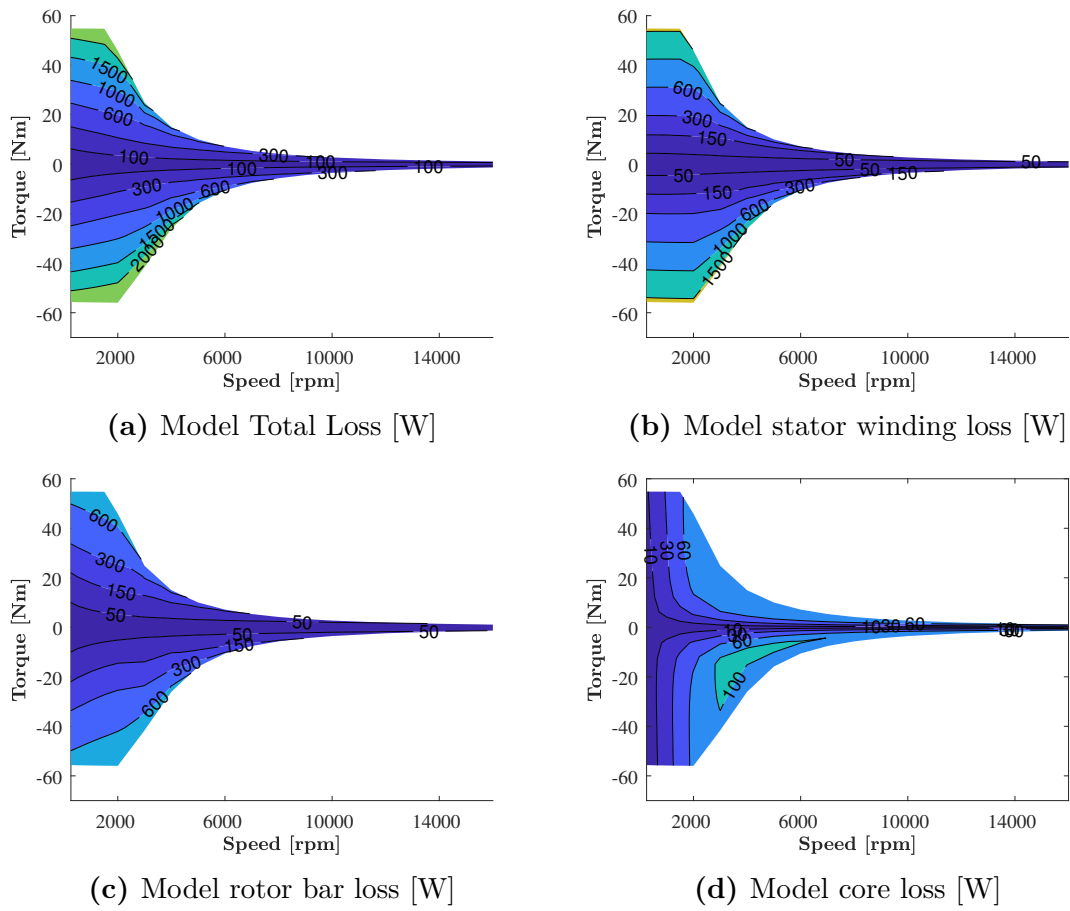


Figure 5.17: Losses in different parts of the 48 V IM from the circuit model

5.3 Efficiency and Torque Comparison between the 48 V IM and the 48 V PMSM

This section presents the performance differences between the 48 V machines in terms of a power map with maximum torque lines, efficiency maps and overall drive cycle efficiencies.

5.3.1 Torque and Power Comparison

The maximum torque curve for the 48 V IM and PMSM are presented in figure 5.18. The PMSM had a higher maximum torque than the IM, 64 Nm compared to 53 Nm during motoring and 64 Nm compared to 61 Nm during generation. Additionally, there was a slight overcurrent for the IM at the maximum torque points. The actual maximum torques were 1-2 Nm lower when within the current limit of 283 A.

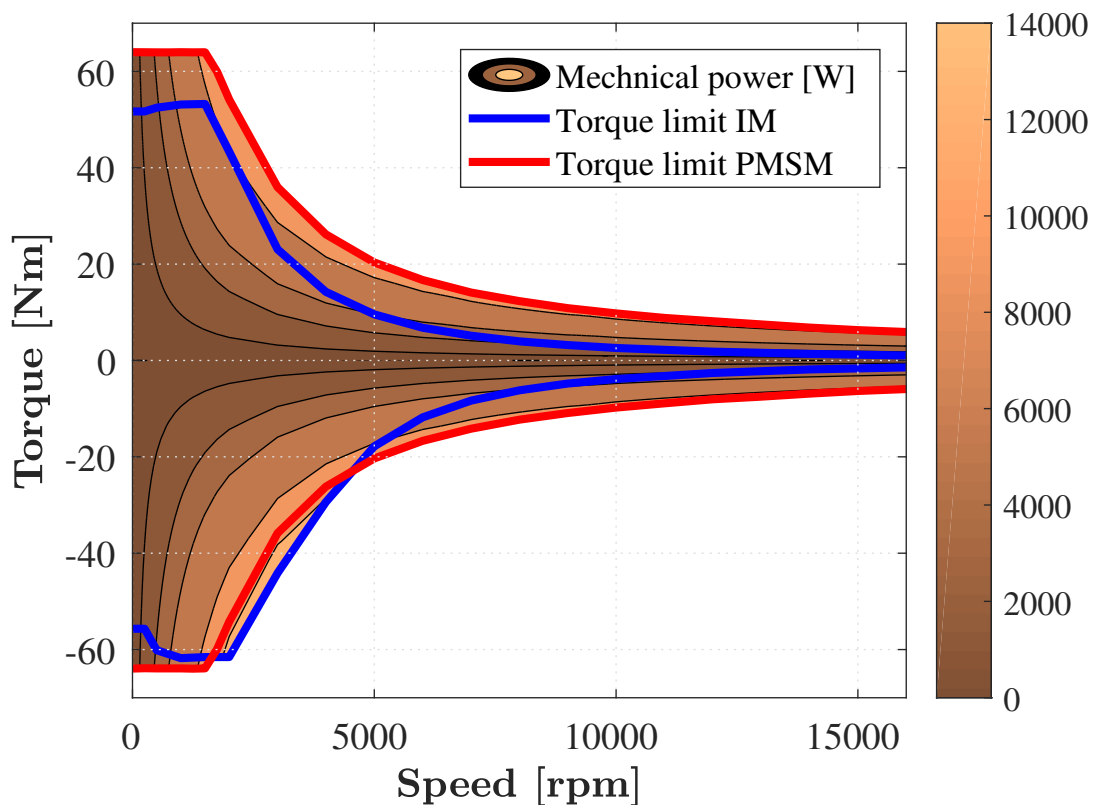


Figure 5.18: Mechanical power and torque limits for the 48 V IM and 48 V PMSM.

The maximum power of the IM was 9 kW during motoring and 13.9 kW during generation. For the PMSM the maximum power was 11.3 kW during both motoring and generation. The point of maximum power occurred at the point where the field weakening started. After the field weakening point, the power should ideally remain

constant. For the PMSM this was almost true. Even at the maximum speed of 16000 rpm the power had fallen with only 9 %. The IM on the other hand was unable to provide a constant power in the field weakening region and the power decreased drastically when the speed increased. At 6000 rpm the IM could provide less than half of the maximum power and only 19 % of the maximum power was available at 16000 rpm.

Between 1600 and 4500 rpm during generation, the IM could provide a higher negative torque than the PMSM. The high leakage inductance of the IM suppresses the terminal voltage and allows for a higher speed at a certain current. However, the high leakage inductance was also the main reason for the rapid power decrease after the field weakening point.

5.3.2 Efficiency Comparison

The efficiency map of the 48 V PMSM is presented in figure 5.19 and the efficiency map of the 48 V IM is presented in figure 5.20. The efficiency of the IM was also obtained with copper instead of aluminium in the rotor bars, which is presented in figure 5.21. In this case the only circuit parameter that was changed was the rotor resistance.

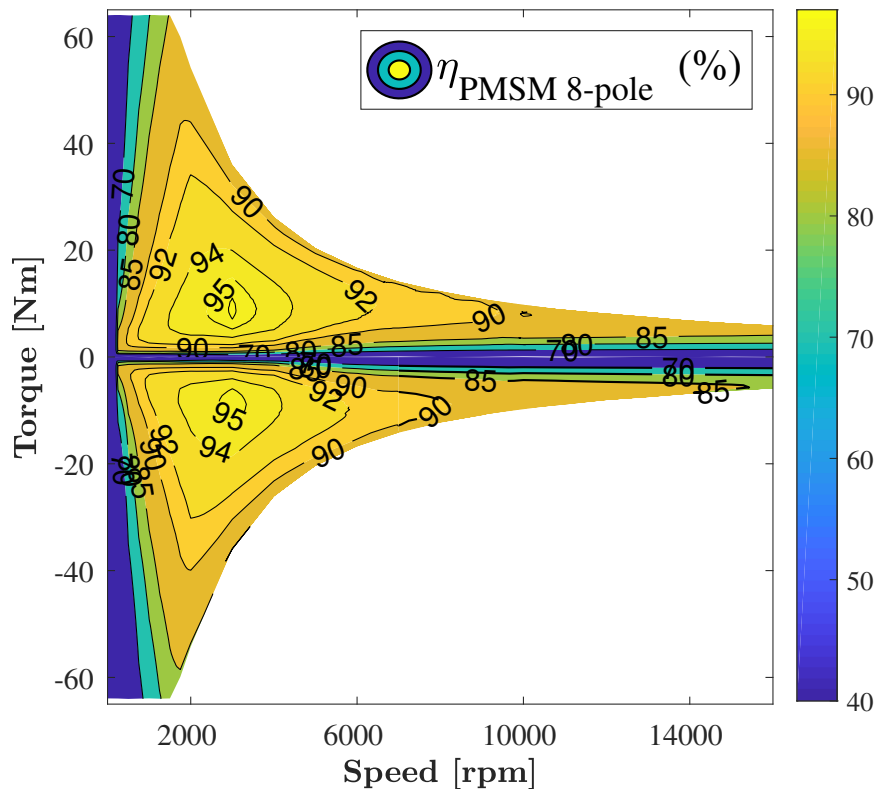


Figure 5.19: Efficiency map of the 48 V PMSM. Field weakening starts at 1 520 rpm.

Using the identification method described in section 3.3.2 the rotor bar resistance was found to be

$$R_{r,cu} = 2.05\Omega.$$

The PMSM had a maximum efficiency of 95 % during both motoring and generation. The maximum efficiencies were substantially lower for the IMs, 87.8 % during motoring and 87.2 % during generation with aluminium rotor bars and 87.9 % during motoring and 87.2 % during generation with copper rotor bars. Figures showing the losses in different parts of the machine can be found in Appendix B for both the PMSM and the IM with copper rotor bars.

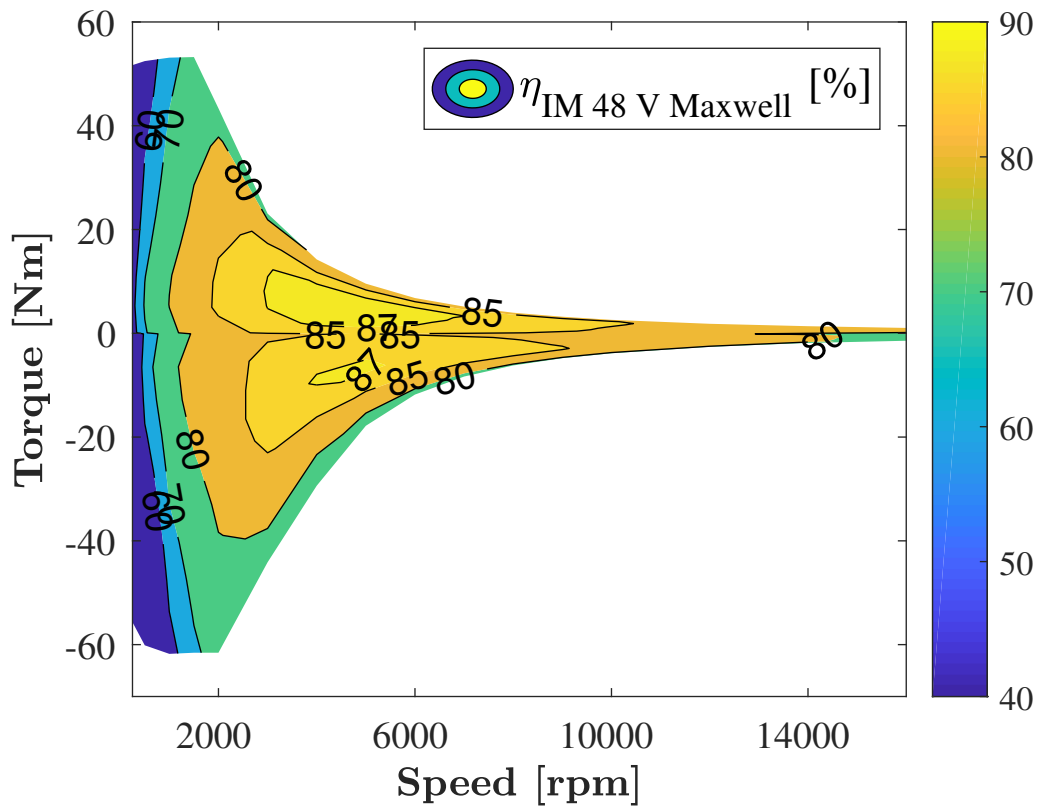


Figure 5.20: Efficiency map of the 48 V IM

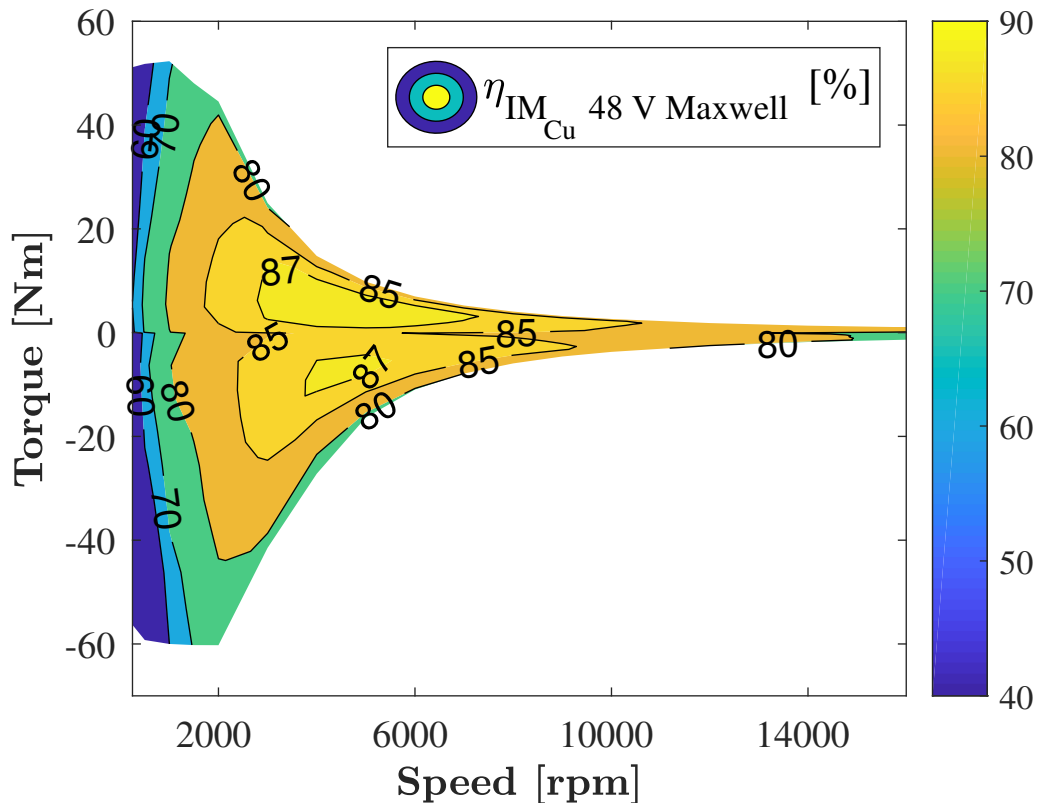


Figure 5.21: Efficiency map of the 48 V IM with copper rotor bars

The difference in efficiency between the IMs and the PMSM was in most regions between 5 to 12 percentage points in favour of the PMSM. Over the whole torque-speed range the only points where the IMs was more efficient than the PMSM were at low torques. At 1000 rpm, the efficiency became higher for the IMs when the torque was below 1 Nm during both motoring and generation. This efficiency break point increased with increasing speed and at 5000 rpm the break point was 3 Nm during both motoring and generation.

The explanation for the PMSM's low efficiency at low torques is that the rotor is always magnetised by the permanent magnets. This led to iron losses that increased with speed even if no voltage was applied. At 1000 rpm the no-load electrical losses were 17 W and at 5000 rpm they were 170 W. In the IM there was no magnetisation of the rotor without any applied voltage and only mechanical losses existed at zero torque.

One interesting finding was that there was only a very small improvement when the rotor bar material in the IM was changed to copper from aluminium, as can be seen by comparing figures 5.20 and 5.21. The resistivity of copper is over 40 % lower than for aluminium. It was therefore believed that the rotor bar losses would decrease by 40 %, which would improve the maximum efficiency by close to 2 percentage points. However, the difference in efficiency was only 0.1 percentage points at the maximum

efficiency point. At high speeds and low torques the overall efficiency improvement was a few tenths of a percentage point. However, for lower speeds the copper rotor bars gave a clear efficiency improvement, especially at high torques. At 500 rpm and 50 Nm the efficiency was 2.5 percentage points higher with copper rotor bars.

It is unknown why the difference was so small for the IMs with different material in the rotor bars. One likely contributing factor is that much of the rotor bar losses came from the harmonics in the rotor. Aluminium also has a larger skin depth than copper, which means that the effective area that the current flows through is smaller with copper and causes higher losses.

5.3.3 Drive Cycle Analysis Comparison

Using the drive cycles presented in section 3.5 the drive cycle efficiencies were calculated according to (3.11). The result is shown in table 5.4. The PMSM was substantially more efficient for both the city and the highway driving cycle, around 5 %.

For η_1 the difference in efficiency between the IM and the PMSM was largest for the city route. One reason for this is that there were a lot of operating points at the upper torque limit due to the way the original drive cycles were changed. In a real driving scenario there would not be as many points at the torque limit and the drive cycle efficiency would therefore increase. The other drive cycle scenario resulting in η_2 gave a clear indication of this. When the operation points outside the torque limit were removed instead of moved, an increase in efficiency could be seen for both machines. The effect was the biggest for the IM during highway driving, where η_2 was 2.2 percentage points higher than η_1 .

Table 5.4: Drive cycle efficiencies. η_1 corresponds to the drive cycle with operation points outside the maximum torque limit moved to the maximum available torque. η_2 corresponds to the drive cycle with operation points outside the maximum torque limit removed.

Drive Cycle	Machine	η_1 [%]	η_2 [%]
Säve highway route	IM	83.1	85.3
	PMSM	88.8	89.5
	IM_{Cu}	83.7	85.6
Lundby city route	IM	84.9	85.3
	PMSM	89.9	90.0
	IM_{Cu}	85.2	85.5
Mixed (25 % city 75 % highway)	IM	83.5	85.3
	PMSM	89.0	89.6
	IM_{Cu}	84.0	85.6

5.4 Sustainability

The sustainability section provides a comparison in material and operational cost of the 48 V IM and the 48 V PMSM. There is also an environmental and social comparison of the two machines with a focus on acidification around the areas of the raw material extraction, as well as the GWP caused by the extraction.

5.4.1 Cost Comparison between IM and PMSM

Table 5.5 presents the material cost and weight of each 48 V machine. The material prices for aluminium and copper were taken from [26]. The prices of the electrical steel and the NdFeB-magnets were inspired by [27, 28] and [28, 29] respectively. The main price difference is that the PMSM uses costly magnets instead of aluminium or copper in the rotor. This makes it over twice as expensive as the IM with the aluminium rotor. The IM uses substantially more copper in the stator. This is mainly due to the shorter end windings in the PMSM since it has 8 poles instead of 4 like the IMs. This also makes the IMs heavier than the PMSM. Changing the rotor bar material in the IM to copper increases the material price with 24%.

Table 5.5: Material cost comparison between the 48 V IM and 48 V PMSM for one machine.

Material	Cost [\$/kg]	Weight [kg]			Cost \$		
		IM	IM _{Cu}	PMSM	IM	IM _{Cu}	PMSM
Aluminium	1.8	0.882	-	-	1.41	-	-
Copper	6.4	3.85	6.78	2.42	26.2	43.4	16.5
Electrical Steel	1.5	8.45	8.45	8.62	12.7	12.7	12.9
NdFeB-magnets	50	-	-	1.06	-	-	53
Total	-	13.2	15.2	12.1	40.3	52.0	82.4

Concerning the price of the NdFeB magnets, the price on the market is varying depending on the concentration of the different elements in the magnets. Two constituents that have a notable impact on the price are the rare earth metals neodymium (Nd) and dysprosium (Dy). Nd makes up around 17 % of the magnet and Dy makes up 4-6 %, with oxide prices of 57 \$/kg and 185 \$/kg respectively [9, 30]. Although, the prices of these rare earth metals spiked in 2011 at 3400 \$/kg for Dy and 300 \$/kg for Nd [9, 10]. Both the rare earth metals are considered a supply risk [11]. Additionally, China controls 90 % of the global supply of rare earths, making any trade greatly dependent on Chinese policies [11]. Therefore, the market for NdFeB magnets must be seen as more uncertain than for aluminium and copper.

To analyse the operational cost of the 48 V machines, the possible cost savings from fuel reduction during operation are analysed. In this analysis only the fuel reduction

caused by the recuperation of the electric machine is taken into account. This is a reasonable assumption since the electric machine is mostly used for regenerative braking, as can be seen in table 3.9 in the case set-up in chapter 3.5. The car is assumed to use diesel as fuel. The value per kWh of recuperated energy is then estimated as

$$Savings\ per\ kWh = \frac{Cost\ of\ diesel}{\eta_{ice} E_{diesel}} = \frac{15.9\ sek/l}{0.34 \cdot 10.25\ kWh/l} = 4.56\ sek/kWh, \quad (5.2)$$

where η_{ICE} is the average efficiency of the ICE taken from [4] and E_{diesel} is the energy content in one litre of diesel taken from [31]. The cost of diesel is taken as the diesel price in Sweden during Mars 2019 [32].

Because of the uncertainties in the assumptions, the recuperated energy price is investigated in a range from 2 to 10 sek/kWh. Using the material cost of each machine in table 5.5 and the energy recuperation per km of the two machines a break even distance is determined. This distance marks the point where the overall cost of the PMSM falls below the overall cost of the IMs and is shown in figure 5.22 for different values per kWh of recuperated energy. The energy recuperation is calculated as

$$E_{recup} = \eta_1 E_{mech,g}, \quad (5.3)$$

with values from the mixed drive cycle and case 1 in tables 3.9 and 3.11 in the case set-up.

Observing figure 5.22, the cost of the IM with the copper rotor surpasses the cost of the PMSM earlier than the IM with the aluminium rotor. The IM with the aluminium rotor surpasses the cost of the PMSM after around 60 000 kilometers if the recuperated energy value is 4.5 sek per kWh. Comparing the two IMs, a driven distance further than 300 000 km makes the IM with the copper rotor overall more cost effective than the IM with the aluminium rotor assuming a recuperated energy value are 4.5 sek per kWh.

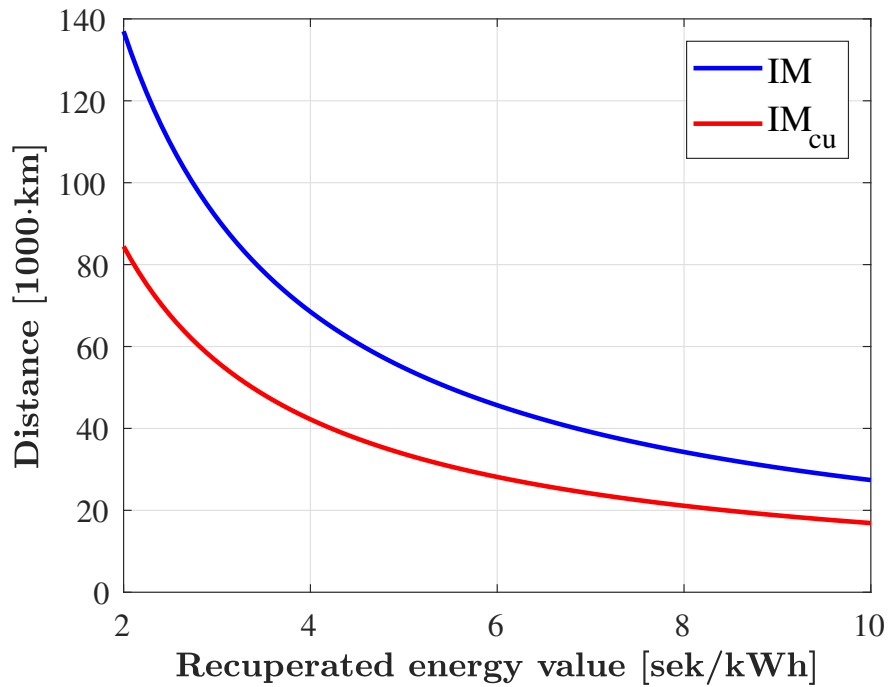


Figure 5.22: The amount of driven km when the overall cost of the PMSM falls below the overall cost of the IM.

5.4.2 Environmental and Social Comparison

The environmental impact of aluminium, copper and NdFeB is divided into two categories; GWP expressed in $kg CO_2, eq$ and acidification expressed in $kg SO_2, eq$. Tables 5.6 and 5.7 present these impacts for production of aluminium, copper and NdFeB-magnets per kg and per 48 V machine. The data for acidification is taken from [33, 30] and the data for GWP is taken from [30, 34, 35]. The values of acidification for the permanent magnets from [30] were converted to $kg SO_2, eq$ by using [36].

Table 5.6: Environmental impact per kg of aluminium, NdFeB and copper.

Environmental impact	Al	NdFeB	Cu
Global warming potential [$kg CO_2, eq$]	12.2	27.6	8.1
Acidification [$kg SO_2, eq$]	0.034	0.657	0.39

Table 5.7: Environmental impact per 48 V machine.

		Al	Cu	NdFeB	Total
Global warming potential [$kg CO_2, eq$]	IM	10.8	31.2	-	42.0
	IM_{cu}	-	54.9	-	54.9
	PMSM	-	19.6	29.3	48.9
Acidification [$kg SO_2, eq$]	IM	0.030	1.502	-	1.532
	IM_{cu}	-	2.64	-	2.64
	PMSM	-	0.944	0.696	1.64

Furthermore, using recycled material can greatly reduce the environmental impacts for both aluminium and NdFeB magnets. According to [30] the impacts reduces to around half in all categories when using recycled material instead of newly mined material for NdFeB-magnets production. The difference is even more significant for aluminium where the GWP is more than 10 times higher for primary production compared to recycled production [37, 38]. In new production the difference of GWP between aluminium and NdFeB-magnets is 12.2 to 27.6 $kg CO_2, eq$ per kg. The difference for recycled production on the other hand is 1.22 to 12.45 $kg CO_2, eq$ per kg. Although, recycled magnets have nearly the same global warming impact as newly produced aluminium, 12.45 to 12.2 $kg CO_2, eq$ per kg. Another factor impacting the emissions from production is geographic location. If aluminium produced in China is excluded from the global average the environmental impact reduces with around a third in all categories [39].

Regarding copper, a time series analysis of the environmental impact of Australian copper production presents greenhouse gas emissions of 2.5 to 8.5 $kg CO_2, eq$ per kg of Cu [40]. A wider geographical analysis shows greenhouse gas emissions varying from 2.4 to 19.5 $kg CO_2, eq$ per kg of Cu [34]. Thereby country and specific location of production are important. The varying emissions also depend on the concentration of Cu in the ore being used for production. An average of the data from [34] results in 8.1 $kg CO_2, eq$ per kg of Cu. The acidification potential of copper production is 0.39 $kg SO_2, eq$ per kg of Cu [33].

Concerning social aspects, the negative impacts connected to mining of rare earth metals are well discussed in scientific articles [5, 6, 7, 8]. The impacts on human conditions are most considerable in China, especially in the region around Bayan Obo. There is pollution from the mines that has reached the Yellow River, which is a primary water source for 150 million people. There are also problems with radioactive material affecting the workers in areas around the mines [8]. On the other hand, the extraction of rare earth elements in Australia and USA has a lower social impact [7].

Also aluminium and copper production have social impacts. Bauxite mining for aluminium production leaves red dust after the mining process that contains heavy metals and other impurities. This can lead to air, water and food pollution in the communities around the mines if not handled properly [41]. Production of copper

5. Result

is connected with toxicity leakage from tailing dams into natural water systems around the mining areas, which leads to human toxicity and freshwater ecotoxicity [28, 34, 42].

6

Discussion

The steady state control algorithm developed in this thesis was based on the inverse gamma model. Considering that the algorithm was not used for dynamic modelling and that long computational time was not a problem, the more accurate T-model could perhaps have given a better result. However, in that case the control would have been more complicated. Another approach that is used for minimum loss control of IMs is to ignore the circuit model all together and instead use a search algorithm that minimises the losses by trial and error [43, 44]. The benefit is that no model parameters are needed and the optimum efficiency is found. The drawback is that the convergence time is long, which implies that dynamic control is not viable. There are however hybrid controls that use a model based control during the transients and switching to a search control algorithm in steady state [43].

An additional possible improvement to the control algorithm would be to modify the torque equation (2.13) so that it would better fit the simulated torque in Maxwell. According to [25] harmonic currents produce a negative torque, which was shown in figure 5.7. This negative torque seemed to have mainly a current dependency. It could then be possible to include an extra current dependant term in the torque equation (3.2) to account for this, meaning the torque and also the efficiency would be better estimated. Another improvement could be to include more stray losses by implementing the extended circuit model presented in [19]. However if this method is chosen, both the circuit parameter extraction and the control algorithm within itself would be much more complicated.

To obtain the initial geometry of the 48 V IM a few important assumptions were made that were not further investigated through simulations. The number of poles, number of stator slots and number of rotor slots are all highly important for the performance of the IM. If the number of poles were increased this could, according to the method used to calculate the initial geometry, increase the maximum torque of the machine. This would also give shorter stator end windings contributing to lower losses and a higher efficiency of the machine.

The improvement of the initial geometry was limited to slot opening parameters and rotor slot parameters. Further improvements can most likely be made if more parameters are included. A different method of optimising could also give better

or faster result. It would be interesting to investigate how a more advanced search algorithm with ability to optimise many parameters simultaneously, perhaps a genetic algorithm could solve the problem. No geometry changes were made when changing the rotor bar material to copper. From the results, copper rotor bars were not a suitable option for the IM in this study, but with some improvements to the geometry this could change.

Although thermal analysis and components other than the motor were excluded in this thesis there are a few things that could be said. The losses in the induction machine were substantially higher than in the PMSM regardless of what rotor material that was used. This favours the PMSM since less cooling is needed to keep the temperature at a reasonable level. Additionally, the torque density was lower for the IM than for the PMSM, meaning a higher current was needed to produce the same torque. Thus, all other components require a higher current rating which increases cost. The inverter losses also increase with increasing current, meaning that the overall system efficiency will be decreased more for the IM than for the PMSM.

One downside of the PMSM discussed in section 5.3.2 is that the rotor is always magnetised. This leads to high iron losses at high speeds even if no torque is produced. One solution is to disconnect the electric machine at high speeds and only run on the ICE. A backside to this is that the mechanics could become more complicated in order to allow this option. The rotor in the IM on the other hand is not magnetised if no voltage is applied, meaning that no electrical high speed no-load losses exist.

In the sustainability analysis only the material of the active parts in the machines was considered. To make a more realistic comparison, all materials as well as the manufacturing of the motor itself needs to be analysed. There are also other factors to take into account, especially under the environmental category. Working conditions, human toxicity, land use and ozon-layer depletion are examples of categories that also could be considered.

7

Conclusion

We believe that the PMSM is the most suitable choice for 48 V mild hybrid applications. The PMSM had a drive cycle efficiency of 88.8-90.0 % while the drive cycle efficiency for the IM was 83.1-85.6 %. The overall power and torque performance were also better for the PMSM than for the IM. The maximum torque of the PMSM was 64 Nm during both motoring and generation, while the IM had a maximum torque of 53 Nm during motoring and 61 Nm during generation. The maximum power was higher for the PMSM in motoring mode, 11.3 kW compared to 9 kW for the IM. In generation mode the IM had a higher maximum power, 13.9 kW compared to 11.3 kW for the PMSM. For the IM the power fell drastically after the field weakening point and only half of the maximum power remained at 6000 rpm. At the same speed, the decrease for the PMSM was only a few percent.

Regarding the sustainability and cost the IM had some benefits. The active material cost was 40.3 USD for the IM and 82.4 USD for the PMSM. However, if the additional fuel savings from the higher efficiency in the PMSM was included the PMSM becomes overall cheaper than the IM after a driven distance of 60 000 km. The environmental impacts of the machines are only slightly better for the IM than the PMSM. The active material PMSM had a GWP of 48.9 *kg CO₂, eq* and an acidification potential of 1.64 *kg SO₂, eq*, while the active material of the IM had a GWP of 42.0 *kg CO₂, eq* and an acidification potential of 1.53 *kg SO₂, eq*. Most of the problems regarding the social aspect were connected to NdFe-magnets and copper production. Since the IM contained more copper but no magnets an advantage could not be given to either the PMSM or the IM.

Changing the rotor bar material to copper instead of aluminium in the 48 V IM was not worthwhile according to the results. The drive cycle efficiency increased at most 0.6 percentage points while both the cost and the environmental impact increased significantly. The cost increased from 40.3 USD to 52 USD, the GWP from 42.0 *kg CO₂, eq* to 54.9 *kg CO₂, eq* and the acidification from 1.53 *kg SO₂, eq* to 2.64 *kg SO₂, eq*.

A steady state control algorithm for the IM was also developed during the thesis. The error between the predicted efficiency and the simulated efficiency in Maxwell was between 0 and 2 percentage points for the 400 V IM with only a few tenths

of a percentage points difference at low speeds. The prediction error for the 48 V machine was higher. At speeds up to 6000 rpm the difference was below 4 percentage points except at the torque limit. Errors in current and torques contributed to this difference. The control algorithm had the most unsatisfactory performance at high speed where the difference between predicted and simulated torque was over 10 percentage points for the 48 V IM. This could be explained by the disregarding of most of the stray losses which have a large impact on the losses at higher speeds [19].

7.1 Future Work

In order to make a complete comparison between the IM and the PMSM for vehicle application a thermal analysis is of great importance on top of the electromagnetic analysis performed in this thesis. Further studies could also improve the comparison by taking the power electronics, cables and mechanics into consideration. Additionally, the steady state minimum loss control developed for the IM could be improved by including more stray losses in the circuit model, or by using a real time search algorithm to find the maximum efficiency without implementing a circuit model.

Bibliography

- [1] S. Larqvist and H. Östergren, “Electric machine comparison for mild hybrid light vehicles with respect to performance and thermal capability,” Master’s thesis, Department of Energy and Environment, Division of Electric Power Engineering, Chalmers University of Technology, 2017.
- [2] The European Commission, “Road transport: Reducing co2 emissions from vehicles,” 2019. Available: https://ec.europa.eu/clima/policies/transport/vehicles_en. Accessed: 2019-05-22.
- [3] The European Commission, “Reducing co2 emissions from passenger cars,” 2019. Available: https://ec.europa.eu/clima/policies/transport/vehicles/cars_en. Accessed: 2019-05-22.
- [4] S. Skoog, “Experimental and model based evaluation of mild hybrid fuel consumption gains and electric machine utilization for personal vehicle application,” in *2017 IEEE Transportation Electrification Conference and Expo, Asia-Pacific (ITEC Asia-Pacific)*, pp. 1–6, Aug 2017.
- [5] S. H. Ali, “Social and environmental impact of the rare earth industries,” *Wealth from Waste: Urban Metal Resources and Industrial Ecology*, 2014.
- [6] B. McLellan, G. Corder, A. Golev, and S. Ali, “Sustainability of the rare earths industry,” *Procedia Environmental Sciences*, vol. 20, pp. 280 – 287, 2014. The 4th International Conference on Sustainable Future for Human Security SUSTAIN 2013.
- [7] S. Holger, Z. Petra, M. Josephine, S. Andrea, V. Sandra, and H. Jürgen-Friedrich, “The social footprint of permanent magnet production based on rare earth elements – a social life cycle assessment scenario,” *Energy Procedia*, vol. 142, pp. 984 – 990, 2017. Proceedings of the 9th International Conference on Applied Energy.
- [8] C. Hurst, “China’s rare earth elements industry: What can the west learn?,” *Institute for the Analysis of Global Security (IAGS)*, no. March, p. 43, 2010.

- [9] M. Riddle, C. M. Macal, G. Conzelmann, T. E. Combs, D. Bauer, and F. Fields, “Global critical materials markets: An agent-based modeling approach,” *Resources Policy*, vol. 45, pp. 307 – 321, 2015.
- [10] M. J. Kramer, R. W. McCallum, I. A. Anderson, and S. Constantinides, “Prospects for non-rare earth permanent magnets for traction motors and generators,” *Jom*, vol. 64, no. 7, pp. 752–763, 2012.
- [11] G. Bailey, N. Mancheri, and K. Van Acker, “Sustainability of Permanent Rare Earth Magnet Motors in (H)EV Industry,” *Journal of Sustainable Metallurgy*, vol. 3, no. 3, pp. 611–626, 2017.
- [12] L. Harnefors, *Control of variable-speed drives*. Västerås, Sverige: Applied Signal Processing and Control, Department of Electronics, Mälardalen University, 2002.
- [13] S. Zhao, H. Yu, J. Yu, and B. Shan, “Induction motor dtc based on adaptive smc and fuzzy control,” in *The 27th Chinese Control and Decision Conference (2015 CCDC)*, pp. 4474–4479, May 2015.
- [14] Technisches Museum Wien [Public domain], “Tmw 50906 schnittmodell einer drehstrommaschine (asynchronmaschine),” March 2011. [Electronic image]. Available: [https://commons.wikimedia.org/wiki/File:TMW_50906_Schnittmodell_einer_Drehstrommaschine_\(Asynchronmaschine\).jpg](https://commons.wikimedia.org/wiki/File:TMW_50906_Schnittmodell_einer_Drehstrommaschine_(Asynchronmaschine).jpg). Downloaded: 2019-04-25.
- [15] O. Wallmark, *AC Machine Analysis, Fundamental Theory*. Department of Electric Power and Energy Systems, KTH Royal Institute of Technology, 2018.
- [16] J. Pyrhönen, T. Jokinen, and V. Hrabovcová, *Design of Rotating Electrical Machines*. John Wiley & Sons, 2 ed., 2008.
- [17] S. Yamamura, *AC Motors for High-Performance Applications*. New York: Marcel Dekker Inc., 1986.
- [18] S. W. Nam and M. N. Uddin, “Model-based loss minimization control of an induction motor drive,” in *2006 IEEE International Symposium on Industrial Electronics*, vol. 3, pp. 2367–2372, July 2006.
- [19] S. Novotny, Donald, Nasar, “High Frequency Losses in Induction Motors,” tech. rep., Dept. of Electrical and Computer Engineering, Madison, WI, United States, 1991.
- [20] T. Thiringer and A. Reinap, “Investigation of a traction induction machine through student works,” *Swedish Electromobility Centre*, 2017.

-
- [21] A. Boglietti, A. Cavagnino, M. Lazzari, and S. Vaschetto, "Preliminary induction motor electromagnetic sizing based on a geometrical approach," *IET Electric Power Applications*, vol. 6, pp. 583–592, November 2012.
- [22] S. Jurkovic, K. M. Rahman, J. C. Morgante, and P. J. Savagian, "Induction machine design and analysis for general motors e-assist electrification technology," *IEEE Transactions on Industry Applications*, vol. 51, pp. 631–639, Jan 2015.
- [23] T. Thiringer, *Measurements and modeling of low-frequency disturbances in induction machines*. PhD thesis, Chalmers University of Technology, 1996.
- [24] K. Bourchas, A. Stening, J. Soulard, A. Broddefalk, M. Lindenmo, M. Dahlén, and F. Gyllensten, "Quantifying effects of cutting and welding on magnetic properties of electrical steels," *IEEE Transactions on Industry Applications*, vol. 53, pp. 4269–4278, Sep. 2017.
- [25] K. Yamazaki, Y. Haruishi, and T. Ara, "Calculation of negative torque caused by slot ripples of induction motors," *IEEE Transactions on Magnetics*, vol. 40, pp. 778–781, March 2004.
- [26] The London Metal Exchange, "Daily prices and monthly averages," 2019. [Online]. Available: <https://www.lme.com/Market-Data/Reports-and-data/Monthly-averages>. Downloaded: 2019-05-27.
- [27] J. Taylor, "What is the price of grain-oriented electrical steel (goes)?," May 2011. [Online] Available: <https://agmetalminer.com/2011/05/12/what-is-the-price-of-grain-oriented-electrical-steel-goes/>. Accessed: 2019-05-29.
- [28] E. A. Grunditz, S. T. Lundmark, M. Alatalo, T. Thiringer, and A. Nordelöf, "Three traction motors with different magnet materials — influence on cost, losses, vehicle performance, energy use and environmental impact," in *2018 Thirteenth International Conference on Ecological Vehicles and Renewable Energies (EVER)*, pp. 1–13, April 2018.
- [29] Adam's Intelligence, "China's exports of ndfeb magnets increased 11% in 2018," February 2019. [Online] Available: <https://www.adamasintel.com/china-ndfeb-exports-increased-2018/>. Accessed: 2019-05-29.
- [30] "Comparative Life Cycle Assessment of NdFeB Magnets: Virgin Production versus Magnet-to-Magnet Recycling," vol. 48, pp. 45–50, 2016.
- [31] European Automobile Manufacturers Association, "Differences between diesel and petrol," 2016. [Online] Available: <https://www.acea.be/news/article/differences-between-diesel-and-petrol>. Accessed: 2019-05-27.

- [32] Statista, “Average monthly diesel prices in sweden from 2016 to 2019 (in british pence per liter),” 2019. [Online] Available: <https://www.statista.com/statistics/857638/average-monthly-diesel-prices-sweden/> Accessed: 2019-05-28.
- [33] P. Nuss and M. J. Eckelman, “Life cycle assessment of metals: a scientific synthesis,” *PLoS One*, vol. 9, 2014.
- [34] A. Beylot and J. Villeneuve, “Accounting for the environmental impacts of sulfidic tailings storage in the life cycle assessment of copper production: A case study,” *Journal of Cleaner Production*, vol. 153, pp. 139 – 145, 2017.
- [35] P. Nuss and M. J. Eckelman, “Life cycle assessment of metals: a scientific synthesis - supportive information,” *PLoS One*, vol. 9, 2014.
- [36] M. Erlandsson, “Miljöbedömningsmetod baserad på de svenska miljökvalitetsmålen - visionen om det framtida hållbara folkhemmet,” Tech. Rep. December 2002, 2003.
- [37] “Environmental consequences of recycling aluminum old scrap in a global market,” *Resources, Conservation and Recycling*, vol. 89, pp. 94–103, 2014.
- [38] “Environment impact analysis of primary aluminum and recycled aluminum,” *Procedia Engineering*, vol. 27, no. 2011, pp. 465–474, 2012.
- [39] P. Nunez and S. Jones, “Cradle to gate: life cycle impact of primary aluminium production,” *The International Journal of Life Cycle Assessment*, vol. 21, pp. 1594–1604, Nov 2016.
- [40] R. Memary, D. Giurco, G. Mudd, and L. Mason, “Life cycle assessment: a time-series analysis of copper,” *Journal of Cleaner Production*, vol. 33, pp. 97 – 108, 2012.
- [41] N. H. Abdullah, N. Mohamed, N. Frisch, and D. Olney, “Potential health impacts of bauxite mining in kuantan,” *The Malaysian Journal of Medical Sciences*, vol. 23, no. 3, pp. 1–8, 2016.
- [42] J. Hong, Y. Chen, J. Liu, X. Ma, C. Qi, and L. Ye, “Life cycle assessment of copper production: a case study in china,” *The International Journal of Life Cycle Assessment*, vol. 23, pp. 1814–1824, Sep 2018.
- [43] E. S. Sergaki and G. S. Stavrakakis, “Online search based fuzzy optimum efficiency operation in steady and transient states for dc and ac vector controlled motors,” in *2008 18th International Conference on Electrical Machines*, pp. 1–7, Sep. 2008.

- [44] A. M. Bazzi and P. T. Krein, “Review of methods for real-time loss minimization in induction machines,” *IEEE Transactions on Industry Applications*, vol. 46, pp. 2319–2328, Nov 2010.

A

M700-50A Core Loss Data

The core material M700-50A was used in both the 400 V IM and the 48 V IM in the Maxwell simulation set-up. The relationship between the core losses P_c and the magnetic flux density B in the material at different frequencies is presented in figure A.1.

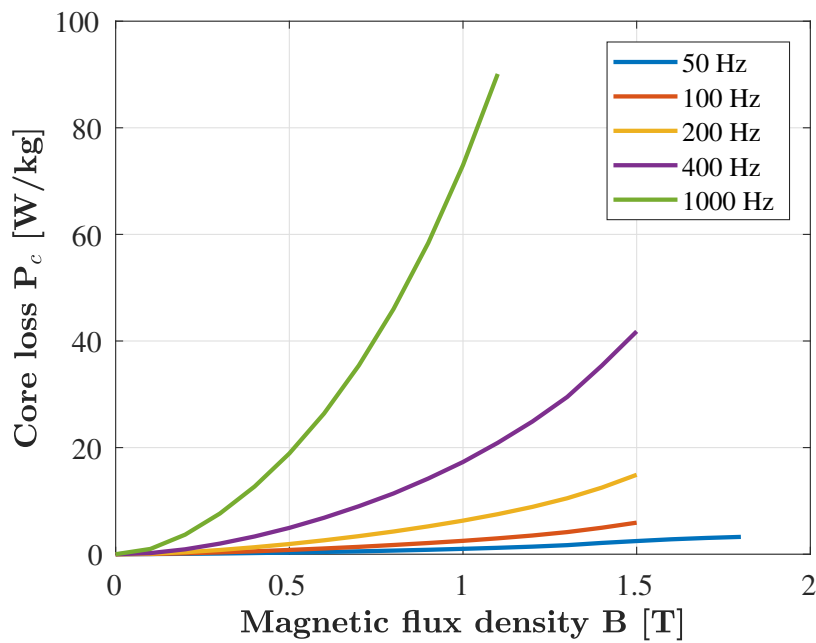
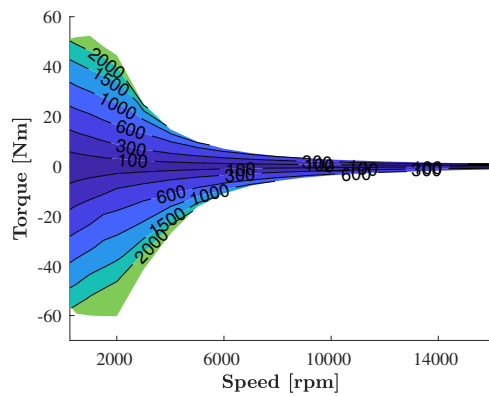


Figure A.1

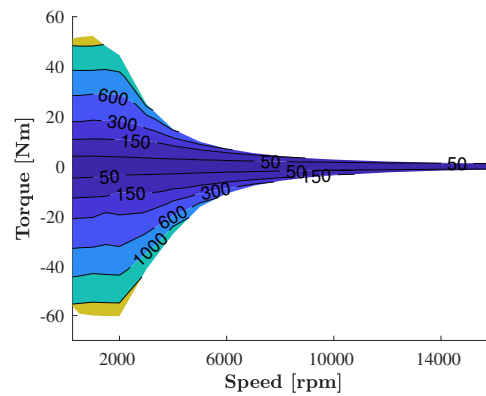
B

Additional Loss Plots for the 48 V Machines

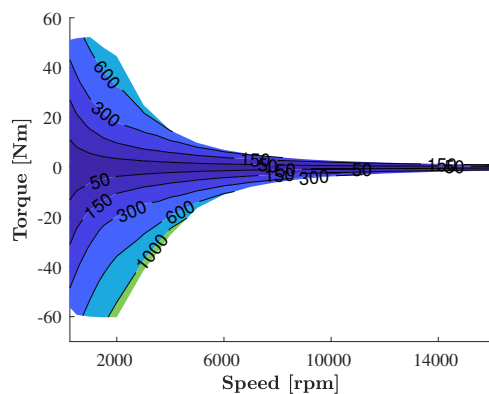
The losses of the 48 V PMSM and IM with copper rotor bars are presented in figures B.2 and B.1 respectively. The losses include stator winding losses, rotor bar losses, core losses and the total losses.



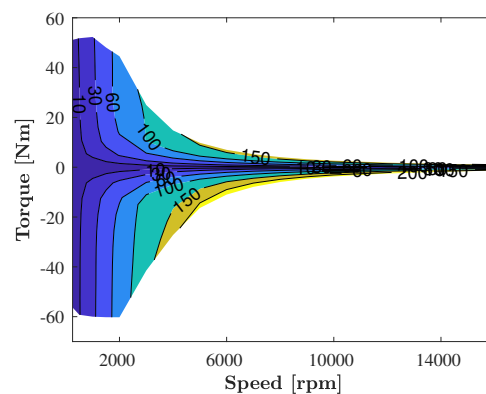
(a) Maxwell Total Loss [W]



(b) Maxwell stator winding loss [W]



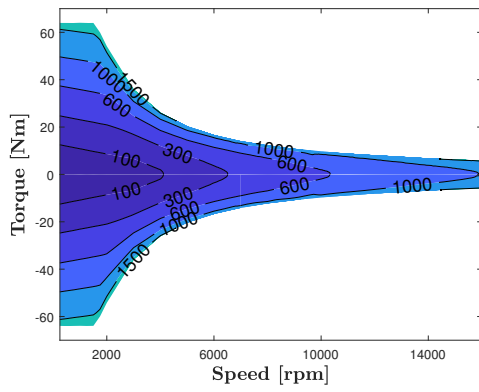
(c) Maxwell rotor bar loss [W]



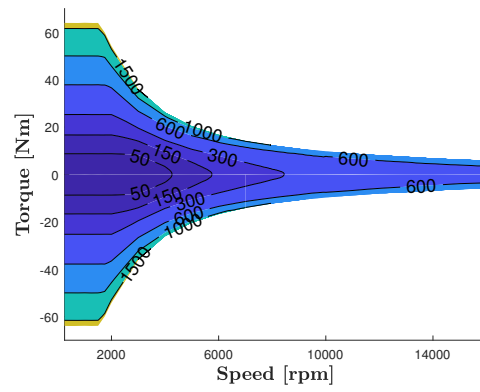
(d) Maxwell core loss [W]

Figure B.1: Losses in different parts of the 48 V IM from Maxwell with copper rotor bars

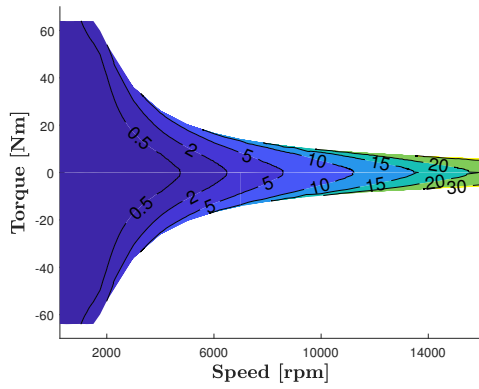
B. Additional Loss Plots for the 48 V Machines



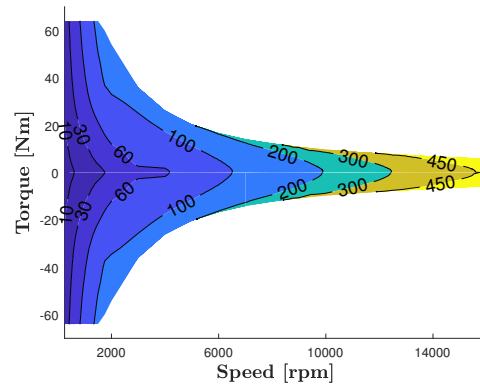
(a) Maxwell Total Loss [W]



(b) Maxwell stator winding loss [W]



(c) Maxwell rotor bar loss [W]



(d) Maxwell core loss [W]

Figure B.2: Losses in different parts of the 48 V PMSM